Masters dissertation

Hardness testing of boron nitride (BN) nano-structures formed by ion beam irradiation.

Author: Mr. LI Lisema

Supervisor: Prof TE Derry Co-supervisor: Dr. M. Madhuku

A dissertation submitted in fulfilment of the requirements for the degree of Masters of Science in Material Science Physics

in the

Faculty of Science, School of Physics

Contents

DECLARATION OF AUTHORSHIP

- This work was done wholly while in candidature for a research degree at this University.
- No part of this thesis has previously been submitted for a degree or any other qualification at this University or any other institution.
- Where I have consulted the published work of others, this is always clearly attributed.
- Where I have quoted from the work of others, the source is always given. With the exception of such quotations, this thesis is entirely my own work.
- I have acknowledged all main sources of help.
- Where the dissertation is based on work done by myself jointly with others, I have made clear exactly what others and what I have contributed myself did.

Signed: 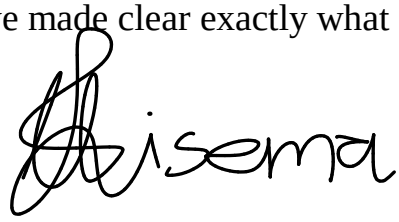

Date: 07 May 2019

ABSTRACT

Hardness measurements on poly-crystalline hexagonal boron nitride (h-BN) ion implanted samples were carried out using the FM-700 (Vickers) micro-hardness tester. Previously, it has been shown that the implantation of h-BN with different ions structurally deforms the irradiated surface layer to cubic-BN nano-particles as revealed by Raman spectroscopy, X-ray diffraction and electron microscopy [1], [2]. In the present study, the h-BN samples were implanted with 150 keV helium (He^+), lithium (Li^+), boron (B^+) and neon (Ne^+) ions at different ion fluences from 1 x 10^{14} to 5 x 10^{16} ions/cm^2, while varying the sample temperature from room temperature to $300℃$. Before and after ion implantation, sample characterization was done with Raman spectroscopy and Glancing Incidence X-ray diffraction (GIXRD) and the hardness measurements taken. The Raman measurements of the virgin h-BN sample has a characterization peak at 1367 cm^{-1} due to the sp^2 hybridized BN planar bonding and after implantation a broad peak around 1300 cm^{-1} is observed on all spectra and it indicates a phase change to cubic-BN, as reported in detail before [3], [4], [5]. The GIXRD results show two peaks at $28.05°$ and $46.45°$ on all implanted samples. The peak at $28.05°$ is the characteristic silicon (311) diffraction peak which came from the sample holder. The peak at $46.45°$ is identified as the (111) peak of c-BN from JCPDS database no 35-1365 and Aradi et al [1]. The micro-indentation measurements indicate that hardness increases with ion fluence from $13.4 \pm 2\ \mathrm{kg/mm^2}$ un-implanted measured value until an optimum value. The Stress σ, Strain $\in$, and Young's modulus E of the implanted were determined from micro-indentation measurements.

To my siblings…

ACKNOWLEDGEMENTS

I would like to express great appreciation to my supervisors Prof. Trevor Derry and Dr. Morgan Madhuku for their continuous support, guidance, earnest motivation and valuable insight of this research work that was made possible because of them. I would also like to thank Dr. Emily Aradi and Dr. Ronald Machaka because their work formed the foundation of this research. I wish to thank Mr. Tony Miller for helping with the ion implantations, Mr. Shadrack Moqabolane for his training on FM-700 micro-hardness tester and the late Dr. Charles Levitt who assisted me with using the Well 3032 Model Diamond Wire saw for sample preparation. Dr. Sanjiv Shrivastava inspired this research by suggesting that micro-indentation measurements would show good results. I also like to express sincere gratitude to Dr. Rudolph Erasmus who help with Raman spectroscopy analysis, Mr. Adam Shnier, Prof. David Billing and Prof. Daniel Wamwangi for the Glancing Incidence X-ray diffraction (GIXRD) measurements.

This research was supported financially by the S.A. Department of Science and Technology - National Research Foundation Centre of Excellence in Strong Materials, and also by the School of Physics, University of the Witwatersrand. Assistance was provided by iThemba LABS (Gauteng), and by the School of Mechanical, Industrial and Aeronautical Engineering and the Raman spectroscopy unit in the School of Physics, both at Witwatersrand University.

Many thanks to my siblings' *ausi* Maggie, Palesa, Makhadi, *abuti* Mokheti, my father Mr Tshabalala, nephews Kwantla and Malefetsane have been a well of inspiration. Each of them have shaped and moulded me, to become the best version of myself in everything that I do.

Thanks to my friends, Mr Maabe and Lobelo for convincing me to pursue this degree, plus by letting me know that if anyone can do it is I! Finally yet importantly Miss Patricia de Jaar, *jy is 'n ster in my lewe*, *dankie.*

Above all, I thank God.

NOMENCLATURE

- BN- boron nitride
- *a*BN- amorphous boron nitride
- *c*BN- cubic boron nitride
- *h*BN- hexagonal boron nitride
- *r*BN- rhombohedral boron nitride
- *w*BN- wurtzite boron nitride
- *t*BN- turbostratic boron nitride
- HPHT- high pressure and high temperature
- dE- energy lost by an ion traversing in matter
- dx- distance traversed
- S- stopping power (subscripts t, n & e denote total, nuclear & electronic, respectively)
- $C(x)$- density of implants/implanted species
- D- dose, fluence, or the number of ions per unit area
- R_p- mean projected range
- ΔR_p- average deviation in R_p
- E_d - displacement energy
- G- Gibbs free energy
- U- internal energy
- p- pressure
- V- volume
- T- absolute temperature
- S – entropy
- PVD - physical vapour deposition
- CVD - chemical vapour deposition
- XRD - X-ray diffraction
- GIXRD -glancing/grazing incidence angle XRD
- TRIM - transport of ions in matter
- m/q - mass–charge ratio

- CCD - charge coupled detector
- d- spacing lattice plane separation
- hkl - Miller index
- FWHM - Full Width at Half Maximum
- TO - transverse–optical phonon mode
- LO - longitudinal–optical phonon mode
- X_d- X-ray depth
- X_L- X-ray attenuation length
- $D_{crystal}$ - estimated crystal size

LIST OF FIGURES

LIST OF TABLES

CHAPTER 1

1. INTRODUCTION

1.1. Motivation

Diamond is not only considered a precious gemstone, it is the hardest material known [6]. However, this description can be misleading to some extent. First, hardness[1], strength[2] and toughness[3] are different properties. Therefore, a material can be strong in one way and weak in the other way. A hard material is difficult to scratch, penetrate through it and has good wear[4] resistance (e.g. diamond and drill bits), thus hardness is a surface property. There are various tests used to measure the hardness of a material: Brinell (BHN), Rockwell (RH), and Vickers (HV) hardness test and, in these measurements, indentation is used. Strength is the internal property of the material; a strong material is difficult to deform (change shape, e.g. steel) and toughness is a combination of strength and ductility[5] (e.g. cast iron). Hence, there are materials that can resist scratching and others can absorb force better (e.g. Diamond is not a tough material but a hard one, because if we apply a force on diamond, it will gradually break but not deform), and one can synthesize materials that combine different properties (mechanical/physical/chemical/ etc.). Diamond has been used for many years and in different applications, the idea of synthesizing a material, which is superior in hardness to diamond, has captured the interest of the materials science community [7]. However, research has shown that to synthesize a stable material that has ultra-hardness superior to diamond is a challenge [3], [4]. Thus, the focus is now shifted to synthesizing materials that have the same phase as diamond but with better properties [3], such as cubic boron nitride (c-BN).

Cubic-BN is a material analogous to diamond and is known to be the second hardest material and has some better properties [8]. Cubic-BN does not react easily with

[1] Hardness is the ability of a material to withstand friction, critically abrasion resistance.
[2] Strength is the amount of force necessary for a material deform.
[3] Toughness the ability of a material to resist breaking when force is applied.
[4] When friction occurs between two surfaces, material lose occurs.
[5] Ability of a material to deform and not break.

ferrous metals, it can be deposited in thin-film form at lower temperatures (300℃ – 400℃) [9], has high resistance to oxidation (at temperatures as high as 1300℃) which makes it more attractive for tooling applications. It is transparent in the infrared and visible part of electromagnetic spectrum; hence, it can be used as protective coating for optical elements. Understanding the parameters that control phase selection in BN is important for research, but there is still a barrier for commercializing c-BN films for technological implementation, because non-cubic BN phases tend to form before c-BN is nucleated [8].

1.2. Problem Statement

The synthesis of cubic-BN and other diamond like phases is usually done under high pressure and high temperature (HPHT) conditions. Research done by R. Machaka [3] and E. Aradi *et.al*. [1] show that when the surface of hexagonal boron nitride (h-BN) is irradiated with positive ions, this can induce a sub-surface layer of c-BN nano-particles near irradiated surface. However, the problem is that the parameters that induce this h-BN to c-BN transformation have not been fully established and the properties of the formed nano-particles have not been determined.

Soft h-BN with a hard c-BN subsurface layer could be very useful. The soft material can be easily machined and a hard layer then added to improve wear resistance. The feasibility of this needs to be further established.

1.3. Objectives

This dissertation reports the experimental work done using ion implantation as a surface technique to induce structural modification to a near surface from a soft h-BN to the ultra-hard c-BN nanoparticles just under the h-BN surface. The main objective is to determine the effects of irradiation by ion implantation of h-BN samples. However, for engineering applications one wishes to answer the questions: Is ion-implanted h-BN harder than unmodified h-BN? Can one measure change in

hardness using the mechanical technique such as indentation testing? Is it too shallow to be useful?

It is problematic to relate results from shallow nano-indentation testing to real engineering situations, which may disturb the surface region to depths of micrometers. However, according to SRIM simulations [1], the penetration depth of 150 keV light ions into h-BN is a few hundreds of nm (e.g. 400 nm for B^+ and 800 nm for Li^+) which puts it within the range of the more applicable micro-hardness testing (e.g. for a 100 g load, a Vickers indenter penetrates about 20 μm). Characterization was done using Raman spectroscopy and X-ray diffraction (XRD).

1.4. Outline

This dissertation is organized as follows: Chapter 2 is a detailed description of the material under investigation, boron nitride. It gives an overview of the structure, properties, applications and the synthesis of hexagonal and cubic boron nitride.

Chapter 3 is on ion solid interactions. It briefly explains ion solid interactions, and the different surface techniques used to modify the surface and characteristics of the material; and it gives an overview of ion implantation and the principles that are behind the transport and propagation of ions in matter. The chapter ends by explaining radiation damage and ion channeling.

Chapter 4 describes the experimental methods and characterization techniques used in this work. A detailed description is given on the instrumentation and the principle of operation for each apparatus used, sample preparation and the experimental procedure details.

Chapter 5 contains the results obtained from the experimental work, and the discussion. The first section of the chapter talks about the results obtained from the computer simulation by Stopping and Range of Ions in Matter (SRIM 2013), followed by Raman spectroscopy, micro indentation, and Glancing Incidence X-ray Diffraction (GIXRD).

Chapter 6 is the summary and conclusion of the dissertation.

CHAPTER 2

2. BORON NITRIDE

2.1. Structure, Properties and Applications

Boron nitride (BN) is a member of Group III-V semiconductors, where one element is from the third (B) and the other from the fifth (N) column in the Periodic Table. In various ways comparable to carbon, BN forms soft sp^2-graphite like and hard sp^3-diamond like bonded phases. Boron nitride has four primary crystalline phases, which are hexagonal, wurtzitic, rhombohedral and cubic-BN (Table 2.1 and figure 2.1). However, two phases are stable (cubic, sp^3-bonded BN and hexagonal, sp^2-bonded BN) [1]. Cubic-BN has a zinc-blende structure, contains tetrahedrally coordinated boron and nitrogen atoms with planes arranged in a three layer (ABC...,) stacking sequence, the structure is a cubic unit cell, containing four boron atoms and four nitrogen atoms. Hexagonal-BN has a HCP (hexagonal close packed) structure with planes arranged in a two-layer stacking sequence (AA'A.,), the h-BN crystal lattice has flat basal planes formed by atoms arranged into the shape of a B_3N_3 hexagonal ring and each ring has three boron and three nitrogen atoms, with each boron atom bonded to a nitrogen atom [8]. Cubic BN has properties like those of diamond, such as extreme hardness, high thermal conductivity, chemical inertness and a wide band gap (E_g~6eV) [1], [2].

Table 2.1: Structural data for boron nitride phases and structural diagrams of the four phases [1].

Structural phase	a(Å)	c(Å)	Atomic positions
hBN	2.50	6.66	B: (0,0,0),($\frac{2}{3}$, $\frac{1}{3}$, $\frac{1}{2}$)
			N: ($\frac{2}{3}$, $\frac{1}{3}$,0),(0,0,$\frac{1}{2}$)
rBN	2.50	9.99	B: (0,0,0),($\frac{2}{3}$, $\frac{1}{3}$, $\frac{1}{3}$),($\frac{1}{2}$, $\frac{2}{3}$, $\frac{2}{3}$)
			N: ($\frac{2}{3}$, $\frac{1}{3}$,0),($\frac{1}{3}$, $\frac{2}{3}$, $\frac{1}{3}$),(0,0,$\frac{1}{2}$)
cBN	3.62	-	B: (0,0,0),($\frac{1}{2}$, $\frac{1}{2}$,0),(0,$\frac{1}{2}$, $\frac{1}{2}$),($\frac{1}{2}$,0,$\frac{1}{2}$)
			N: ($\frac{1}{4}$, $\frac{1}{4}$, $\frac{1}{4}$),($\frac{3}{4}$, $\frac{1}{4}$, $\frac{3}{4}$),($\frac{1}{4}$, $\frac{3}{4}$, $\frac{3}{4}$),($\frac{3}{4}$, $\frac{1}{4}$, $\frac{3}{4}$)
wBN	2.55	4.42	B: (0,0,0),($\frac{1}{3}$, $\frac{2}{3}$, $\frac{1}{2}$)
			N: (0,0,$\frac{3}{8}$),($\frac{1}{3}$, $\frac{2}{3}$, $\frac{7}{8}$)

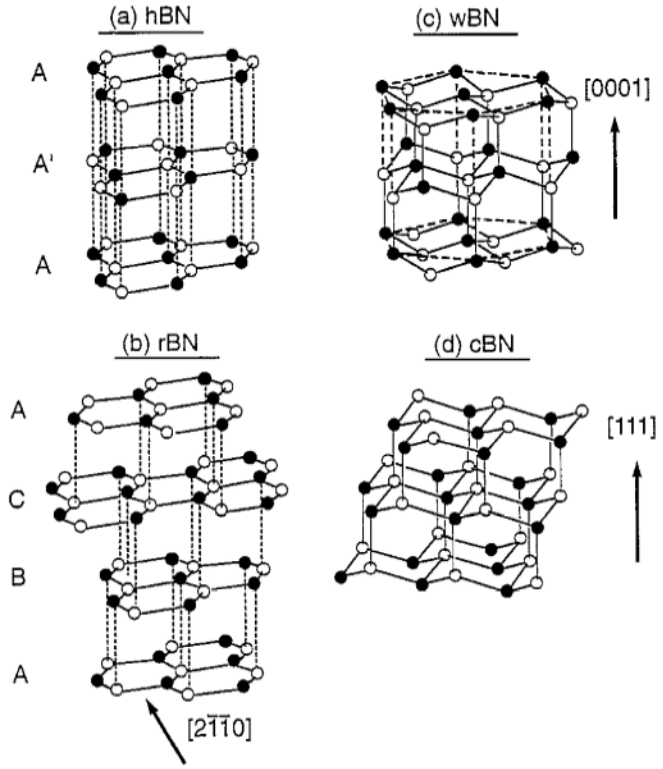

Figure 2.1: Structures of the $\boldsymbol{sp^3}$-bonded phases c-BN and w-BN and the $\boldsymbol{sp^2}$-bonded phases h-BN and r-BN [2].

2.1.1. Phase stability

Cubic boron nitride is synthesized in bulk by means of high pressures and temperatures. The pressure-temperature (P-T) phase diagram (figure 2.2) gives graphical representation of the state and phases of equilibrium at any given pressure and temperature condition. The Gibbs free energy, *G*, equation 2.1, is what determines the stability of a phase, where *U* is the system internal energy, *p* is the pressure, *V* the volume, *T* is the absolute temperature and *S* is the system entropy. As already mentioned BN has several allotropic phases, but for the purpose of this dissertation we are interested in the stable phases c-BN and h-BN and their phase diagrams. From the phase diagram, is observed that c-BN is thermodynamically stable up to temperatures of 1600 K. Since c-BN and h-BN phases are the stable forms under ambient conditions, thus, under a given condition of pressure and temperature, c-BN and h-BN can coexist (where the Gibbs free energy is zero), but only one of the phases is stable, with minimal free energy, while the other is metastable [1], [2].

$$G = U + pV - TS \tag{2.1}$$

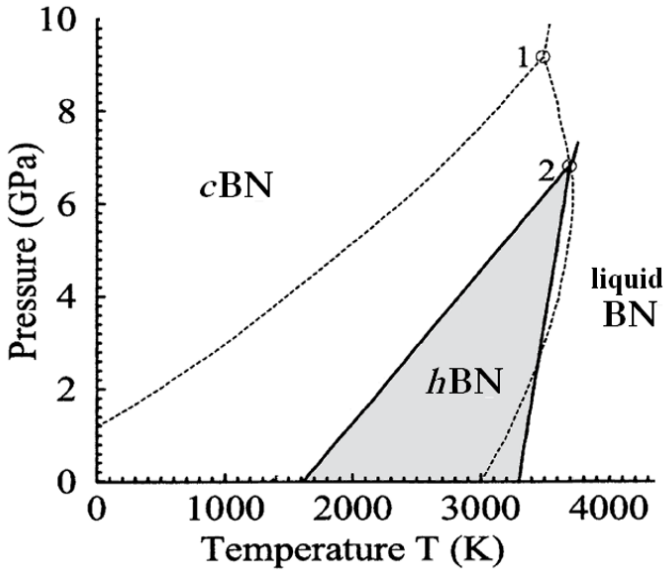

Figure 2.2: Phase diagram of boron nitride (solid line (2)) and the Corrigan–Bundy phase diagram (dotted line (1)) [10].

2.2. Synthesis of Boron Nitride

When synthesizing boron nitride on an industrial scale, one of two processes is involved, namely ammonolyisis process of boron oxide at high temperatures of $1000℃$ and nitridation [11], [12]. The first reaction, is melting boron oxide with ammonia and the second is the melting of boric acid with urea[6], guanine[7] and melamine[8] [13]. The following is the chemical reaction involving ammonia and boric acid:

$$3B(OH)_{2(s)} + 3NH_{3(g)} \rightarrow 3B(NH_2)_{(s)} + 6H_2O_{(l)} \quad (2.2)$$

After heating to temperatures of about $1000℃$ the reactions yields,

$$B(NH)_{2(s)} \rightarrow 2NH_{3(g)} + BN_{(s)} \quad (2.3)$$

Combining boron nitride powder in nitrogen plasma at $5500℃$ yields hexagonal-BN, h-BN can be produced by hot pressing BN powder using boron oxide as a sintering agent [14]. In this dissertation, the focus is limited to the synthesis of h-BN but the other allotropic forms of BN have been synthesized from h-BN as a starting material. [14], [15], [16].

2.3. Hexagonal Boron Nitride

Hexagonal boron nitride (h-BN) is often referred to as white graphite, (h-BN is transparent as a single crystal, but appears as a white solid when compressed) because it has a similar structure and bonding to that of graphite and is one of the most used BN forms in industries [17]. It has a density of $2.27\ g/cm^3$ and it is made of hexagonal rings where each layer has a flat network of B_3N_3 (with every boron atom bonded to a nitrogen atom) hexagons [18]. However, hexagonal-BN has layered structure like graphite with the exception that, hexagonal rings of the basal

[6] Known as carbamide, is an organic compound with chemical formula $CO(NH_2)_2$

[7] Is one of the four main nucleobases found in the nucleic acids DNA and RNA, the others being adenine, cytosine, and thymine

[8] An organic base and a trimer of cyanide with a 1, 3, 5,-triazine skeleton.

planes are positioned directly above each other and rotated by $180°$ between alternate layers thus the stacking sequence can be described as AA'A. The in-plane atoms are bonded by localized sp^2 hybridization, while the out of plane are atoms bonded by de-localized weak π-orbitals. The electrons in π-orbitals are localized closer towards the N-atom than B-atoms, and this feature makes h-BN to be an electrical insulator [19]. Therefore, the N atom gains 1-3 electrons from its three neighboring boron atoms. The inter-planar layer is a mixture of the weak van der Waals bonding and ionic attraction between the oppositely charged ions in the adjacent planes [20], [21].

The a-lattice parameter of h-BN is greater than that of graphite and the c parameter is smaller, because the two compounds bond differently. The C-C bond in graphite is covalent and is much stronger and thus shorter than the B-N bond which is partially ionic and covalent, thus, the intralayer interaction is reduced and the electrostatic interlayer (Van der Waals interaction) strengthened. In this way the interlayer distance c of h-BN is smaller than that found in graphite [19].

Hexagonal-BN has been used extensively in industries as well as in research in vacuum technology and in electronics [2], because it is a good electrical insulator that has good thermal conductivity and stability. It has been used as a lubricant in many industries. Normally when c-BN is synthesized h-BN is used has a starting material.

2.4. Cubic Boron Nitride

Cubic-BN crystallizes in a zinc-blende structure [9], it contains tetrahedrally coordinated boron and nitrogen atoms with planes arranged in a three layer (ABC...,) stacking sequence [22]. The structure in figure 2.3 is a cubic unit cell, containing four boron atoms and four nitrogen atoms. Each boron is tetrahedrally bonded to four nitrogen atoms (sp^3-hybridization) and this structure has a lattice parameter of $a = 3.62$ Å, and a density of 3.49 g/cm^3 [23]. The c-BN structure is composed of two FCC sub-lattices, shifted over one quarter of the lattice along the diagonal

[9] Zinc-blende structure is the same as diamond, except that the two atoms forming the basis of FCC, face centered cubic, lattice are different.

direction. Pure c-BN is transparent or amber in color, with different colours occurring with introduction of defects or excess boron or nitrogen [24].

Cubic-BN is now known as the most stable phase of BN under ambient conditions. If a material can form strong covalent bonds, a low coordination is favoured due to Pauli Exclusion Principle and electrostatic repulsion between the charges. Therefore, the C-C bond is neutral, and carbon is stable in the layered graphite structure. The B-N bond is partially ionic and partially covalent, in a way the h-BN structure is polar as compared to the c-BN structure (c-BN is electrochemically favoured). Table 2.2, gives a summary of some of the properties of c-BN and diamond. These properties make c-BN very useful in many industrial applications. Its amazing combination of mechanical, physical, chemical, and thermal properties make it desirable for use in cutting saws, drill tips, grinders, dies, and wear resistant coatings. The optical and electronic properties make c-BN a promising material in the semiconductor industry in applications such as diodes, heat conductors and heat sinks [24].

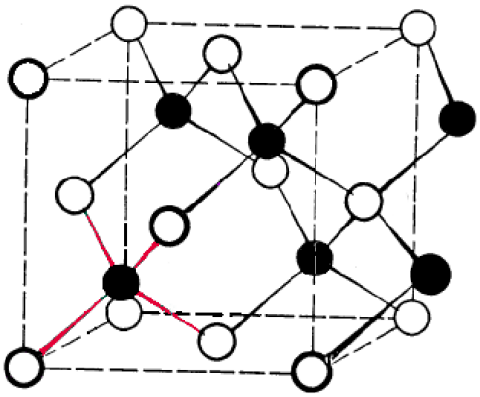

Figure 2.3: The structure of c-BN [2].

2.4.1. Synthesis of Cubic Boron Nitride

BN was commonly crystallized in a sp^2 graphite like form and this led to speculations that boron nitride might exist in diamond like form [23]. However, it was discovered that high pressure and high temperature conditions, similar to those found effective for diamond synthesis, were suitable for producing diamond like c-BN. When h-BN is the starting material and conditions are thermodynamically stable, the cubic-BN form can be produced by means of catalyst action. The catalysts which are effective for the formation of cubic boron nitride are different from those required for diamond synthesis, and consist of the alkali and alkaline-earth metals, their nitrides, and antimony, tin, and lead [25].

Direct High-pressure High Temperature (HPHT) synthesis:

The HPHT synthesis method was first used in 1956 as a primary method for c-BN synthesis through direct solid-state transformation of low-density BN phases like h-BN [26]. The conditions to achieve h-BN to c-BN transformation are pressure of 12 GPa and temperature of 2000 K (this is where the BN phase diagram shows c-BN stable and the low dimensional phases are metastable). A very high activation energy barrier [27], [26] prohibits a direct transformation of h-BN to c-BN. Thus, the thermobaric conditions at which transformation occurs far exceed the phase diagram equilibrium conditions.

The Gibbs free energy (equation 2.1) determines the stability of the system. As the pressure and temperature increase, the phases with lower molar mass volume are favoured even if they have high internal energy. When high pressure and high temperature are applied to low-density modifications of BN phases, h-BN reduces the Gibbs free energy hence there will be reduction in its molar volume and therefore structural modifications to cubic form [1]. High temperature overcomes the energy barrier while the high pressure modifies the electronic and structural bond arrangement of the h-BN material [26] .

Indirect c-BN Synthesis:

This method, involving the use of multicomponent catalyst-solvent, is presently the method of obtaining c-BN on industrial scale. Different solvents can be used instead of using the extreme conditions used in direct synthesis. Hexagonal-BN is partially dissolved into a solvent precursor material forming a eutectic melt mixture when high pressures and temperatures are applied to the composition. The formation of c-BN leads to precipitation from the composition. Solvents precursors are normally alkali and alkaline earth metal nitrides of general formula X_3N_2 (e.g. Mg_3N_2) and some BN alkali and alkaline earth compounds shown to be catalysts are Li_3BN_2, $Mg_3B_2N_4$, and $Ca_3B_2N_4$. It has been reported that alloys such as Fe-Al, Ni-Al, Mg-Al and Ag-Cd are effective catalyst-solvents for the h-BN to c-BN phase transformation. JY Huang and co-workers [28], [29] have also investigated using amorphous boron nitride as the starting material instead of hexagonal boron nitride and c-BN formation could be observed at lower pressure(p), temperature (T) values. Water molecules adsorbed at the surface of the starting material have been observed to be having a catalytic effect in the transformation: the transformation at the surface has been observed to occur at much lower *p*, *V* conditions than the bulk of the material [22], [28], [29].

Table 2.2: Comparison of the physiochemical properties of cubic boron nitride and diamond [23].

	c-BN	Diamond
Structural properties		
Structure	Cubic F_{43m}	Cubic F_{d3m}
Unit cell parameter (Å)	a=3.615	a=3.567
Interatomic distance(Å)	d=1.57	d=1.54
Density(g/cm^3)	3.48	3.52
Chemical Properties		
Doping elements	B, Be, S, Si, Al	B, P
Reaction with Fe Materials	Inert	Forms (Fe_3C_2)
Mechanical Properties		
Hardness (kgmm^{-2})	4500	9000
Knoop hardness (Gpa)	73	115
Bulk modulus (GPa)	847	1141
Thermal Properties		
Conductivity (Wcm^{-1}K^{-1})	13	20
Expansion (^{o}C $^{-1}$)	4.8	3.5
Oxygen stability (^{o}C)	1200	600
Phase change temp. (^{o}C)	1500	1400
Melting Point (^{o}C)	2967	3726
Breakdown field (MV cm^{-1})	8	3.1
Optical Properties		
Refractive index	2.117	2.417
Band gap(indirect)(eV)	6.1-6.5	5.47
Electrical Properties		
Resistivity (Ωm)	10^{10}	10^{16}
Dielectric constant	7.1	5.50

Ion Beam Assisted Deposition (IBAD):

IBAD is an alternative method for synthesizing c-BN at low pressures and temperature conditions. It involves the use of high voltage, and ion beam bombardment applied to the h-BN substrate. Low energies from 0-1keV are used to produce high compressive stress in the h-BN substrate, therefore, enhancing the phase transformation to the cubic form. IBAD is a group of processes, which include Physical Vapor deposition (PVD), Chemical Vapour Deposition (CVD) , Radio Frequency Sputtering, among others [30], [31].

PVD is when boron is thermally evaporated onto the h-BN sample and immediately bombarded with nitrogen and argon ions, producing boron and nitrogen interstitials in the material and the boron atoms will be driven into the lattice by the argon ions. The interstitial atoms condense to create AB-planes in h-BN, leading to an increase in the density and altering the sample to cubic form [32], [33]. PVD has different forms that have been used to synthesize c-BN (plasma deposition, Ion Plating PVD, Pulsed Laser Ablation PVD, mass selected ion deposition, ball milling, and magnetron sputter PVD) [34].

The CVD is similar to PVD except that gaseous precursors ($B_2H_6, BH_3NH_3, H_2, F_2$ and trimethyl borazol) are used instead of solid ones used in PVD, and reagents are deposited on the h-BN sample at temperatures of about 100-1000℃. The CVD processes used to produce c-BN are Radio-Frequency plasma CVD, Laser CVD, Jet Plasma CVD and microwave plasma CVD/Cyclotron Microwave plasma CVD (which produces a thick c-BN film) [34].

2.4.2. The Hexagonal-cubic BN Phase Transformation.

There are two types of mechanisms for direct transformation from the low-density phase to the cubic-BN phase: diffusion-less martensitic transformation and diffusional transformation. Martensitic is a type of transformation involving well-crystallized (stable) starting material (e.g. h-BN and r-BN). Diffusional is a type of transformation involving poorly crystallized starting material [35], [36].

What distinguishes the two mechanisms is that in diffusional, changes take place by atom-to-atom interactions (nucleation) in such a way that the neighbour atoms are not neighbours after the transformation. In martensitic, the atoms rearrange but retain their neighbours after the transformation but at an altered separation, this is known as diffusion-less mechanism [29].

Given a comparison of the steric arrangements in h-BN and c-BN, it is clear that the phase transformation from h-BN to c-BN is diffusionless. This transformation undergoes what is known as 'buckling and stretching of basal hexagons' [2]. When under pressure the flat (0001) B_3N_3 (Hexagonal) basal layers lose their flatness (change shape) resulting in changes in electron density in the interatomic and interlayer spaces. The electron density between B-N bonds will decrease; this will increase bond length, as the bond will be weak. Meanwhile, the electron density between the boron and nitrogen atoms in adjacent layers will increase in way that decreases the local interlayer spacing; and as a result, a bond will form. The bonding is now tetrahedral [2].

CHAPTER 3

3. ION SOLID INTERACTIONS

3.1. Introduction

Ion-solid interactions is a field of material science where high-energy particles are accelerated onto the surface of a solid material and this causes radiation (e.g. Photons) and particles (e.g. electrons) to be emitted and analyzed with different characterization techniques. The physics of ion-solid interactions was unveiled when J.J Thompson and Niels Bohr designed experiments showing how particles penetrate, slow down and stop in matter [1]. Processes involved in ion-solid interactions are substrate sputtering, ion Beam Assisted Deposition (IBAD), ion beam mixing, ion implantation and ion induced phase transformation. The interaction of any material surface with the environment plays a huge role (e.g. friction, oxidation etc.), that is why ion-solid interactions techniques are crucial because they can modify the surface and characteristics of the material to make better, so that the material can withstand the harsh environmental conditions. Ion beams have been used mostly in Nuclear Physics, where the interaction with a detector material makes it possible for the identification of unknown particles and their properties. Ion implantation is used throughout this dissertation and is important in semiconductors to introduce dopants into materials, such as silicon (Si), germanium (Ge), gallium nitride (GaN) and gallium arsenide (GaAs). Ion irradiation has also been used in ion induced phase transition; a good example is the phase transformation from graphite to diamond and h-BN to c-BN [37], [38].

3.2. Ion Implantation

Ion implantation is used to introduce ions of an element into the surface of a solid material by accelerating desired ions (in energy range of electron volt to mega-electron-volt) onto the material. Most of the ions will come to rest in a shallow surface layer of the target material, making defects in the stopping process. The interaction of the created point defects with the material changes the properties of the implanted material. Ion beams have been used to synthesize new metastable phases that are not attainable by other techniques (e.g. semiconductor material doping). Ion implantation has been used successfully to alter various properties of different target materials, because it has many advantages than other surface modification techniques such as coating, diffusion and oxidation. The implantation depth can be controlled and it is possible to control the ion concentration by changing the energy and ion fluence, thus, a precise selection of the energy and fluence can develop a desired impurity profile. It is also a low temperature process, therefore, there is no change in the size of the material due to thermal alterations hence minimal surface degradation [39].

The disadvantage of ion implantation is that many atoms are displaced from their positions causing radiation damage, which may be undesirable in semiconductor modifications. However, this damage can be annealed away in materials like silicon and germanium. The damage can be useful in altering the properties of other materials like h-BN [1].

3.2.1. Concepts of Ion Implantation

Implant fluence:

The implant dose (*D*) is the number of ions implanted per unit area (cm^2) of the specimen, when the beam current (*I*) scans the surface of the specimen for a specific time (*t*). The total implanted charge (*Q*) collected is obtained by integrating the beam current and is given by the following equation:

$$Q = \int_{t_0}^{t_1} Idt \tag{3.1}$$

Therefore, the fluence (D), (ions/cm^2) is equal to the total implanted charge, *Q*, over the cross-sectional beam area (*A*), times the ion charge (q_i). The following equation is obtained:

$$D = \frac{Q}{q_i A} \tag{3.2}$$

3.2.2. Projected range (R_p)

When the ions interact with the sample, they lose energy and change direction either by colliding with the electrons or nuclei of the specimen. Therefore, the stopping power (*S*) of the target material is defined as the energy loss (*E*) per unit path length (*x*) of the ion (it consists of two components, nuclear stopping power S_n and electronic stopping power S_e), as described in equation 3.4). These collisions are random, because of this; the length x measured along the ion path (total range, *R*) or along the beam direction (projected range, R_p) are random variables [2]. Projected range simply means the depth where most ions stop, figure 3.1. The distribution of the implanted ions about that depth (R_p) can be approximated as Gaussian with a

standard deviation (ΔR_p). In theory, the ion concentration can therefore be written as [39], [40]:

$$C(x) = C_p e^{\left(-\frac{(x-R_p)}{2\Delta R_p^2}\right)}, \tag{3.3}$$

where C_p is the peak concentration, and is given by $\frac{D}{\sqrt{(2\pi\Delta R_p^2)}} \cong \frac{0.4D}{\Delta R_p}$. The SRIM® computer program can be used to perform TRIM Monte Carlo calculations in order to determine distribution and collision details of the ion and recoil atoms.

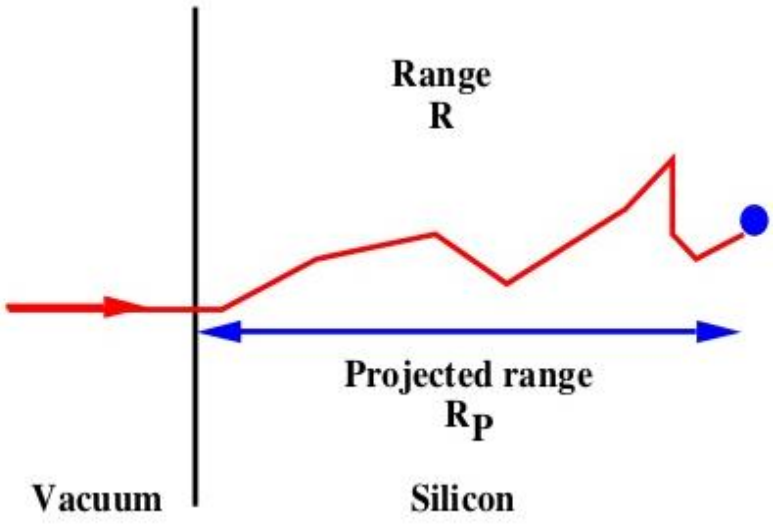

Figure 3.1: Diagram showing the depth where most ions stop (Projected Range) [41].

$$S = -\frac{dE}{dx} = S_n + S_e \tag{3.4}$$

From equation 3.4, $S_n = \left(\frac{dE}{dx}\right)_n$ and $S_e = \left(\frac{dE}{dx}\right)_e$.

Electronic stopping:

As briefly mentioned, electronic stopping is inelastic collision between the implanted ion and the electrons of the target atoms. The collisions can cause excitations and ionization of the target atom. When the ion interacts with the target atom clouds of electrons it will slow down, because the ion will be stripping the negative charge of the electrons as it moves through the sea of electrons. Thus, the ion will slow down with each additional electron it picks up until it is almost neutralized. At the end of the range the ion is neutral (low ionization state). This leads to distribution of ranges.

From figure 3.2, literature shows that the electron stopping power (S_e) at is related to energy E by the following expression [2], [39].

$$S_e \propto E^{\frac{1}{2}} \tag{3.5}$$

Electronic stopping reaches a maximum at implant velocities comparable to Bohr velocity, v_o (m/s) of the valence electrons of the target atom.

Nevertheless, when the electronic stopping decreases, as the ion is stripped of electrons by the target atoms, it falls in the regime of the Higgs boson energies [42], which are not relevant for the work of this dissertation.

Nuclear stopping:

When the ion has slowed down, the electronic stopping becomes small. As result, nuclear interaction will start dominating the ion stopping process. As already, mentioned nuclear stopping is elastic collisions between the ion and target nucleus but is considered an interaction between two nuclei.

In Fig. 3.2., the nuclear stopping power is related to energy by the following expression [39] :

$$S_n \propto -E^{-2} \tag{3.6}$$

Nuclear interactions are responsible for the huge damage of the specimen lattice structure.

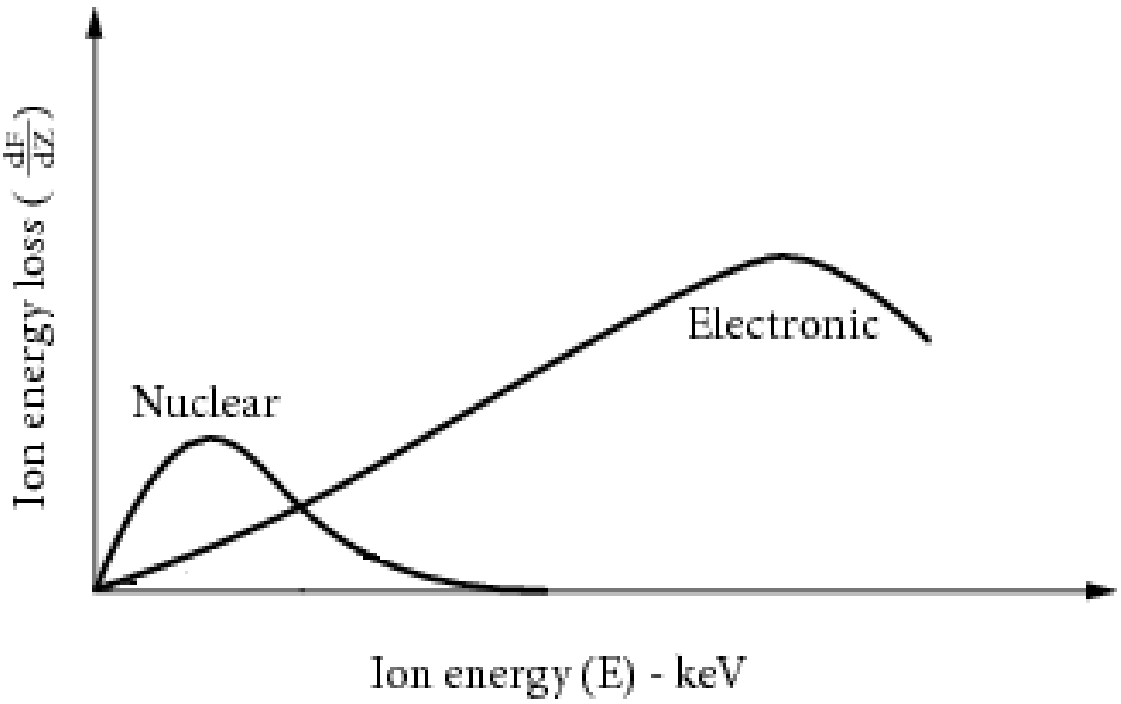

Figure 3.2: Nuclear and electronic components of the ion stopping power as a function of ion energy [39].

3.3. Radiation damage

The projectile ion makes many collisions with target atoms by breaking chemical bonds and displacing them from their lattice sites. The interruption of the existing lattice atomic arrangement by the projectile ion is known as *Radiation Damage*. Therefore, if the energy of the ion is more than the displacement energy E_d (the energy required to create a Frenkel pair) of that material then the atom is displaced from its lattice site leaving a vacancy. When the recoil atom has energy greater than E_d, it will further cause creation of Frenkel pairs and this is known as a *displacement spike* because it is a collision cascade that is characterized by a huge volume of Frenkel pair defects. But when the recoil energy drops below E_d, the projectile won't be able to knock off the target nuclei from their lattice positions, instead they will lose energy through collisions that will cause amplitude vibrations without leaving their lattice sites. The collision induced vibration energy is shared by the neighbouring nuclei and appears as a source of heat. This is known as a thermal spike and normally develops in a plasma-like structure and lasts for about ~$10^{-12}s$ [35]. Thermal spikes occur at the centre of displacement spikes.

The radiation damage also depends on the ion implantation conditions like the implantation fluence, temperature, and the properties of the target material as well as the mass of the projectile ions. For example, defects that are normally created like interstitials or vacancies can interact during and after ion implantation to form disordered regions that extend over a large region of the target in the form of dislocation loops, grain boundaries, impurity clusters, voids, crystalline inclusions or gaseous inclusions. The defects are normally controlled by the temperature at which implantation is done or at which the sample is annealed as well as the defects migration energies. Literature shows that there exist different temperature regimes that control the movement of point defects in the damage cascade caused by the implanted ion [35]. At low temperatures, ~ 320K in diamond, all the point defects are immobile. At high temperatures, ~320K-800K in diamond, the interstitials become mobile while the vacancies remain immobile, but at higher temperatures, more than 800K, all the primary defects are mobile [35]. Generally, the movement of interstitials is more than that of vacancies. However, if the primary defects cluster

and form secondary defect agglomeration or dislocation loops they become immobile and more stable even at high temperatures [35].

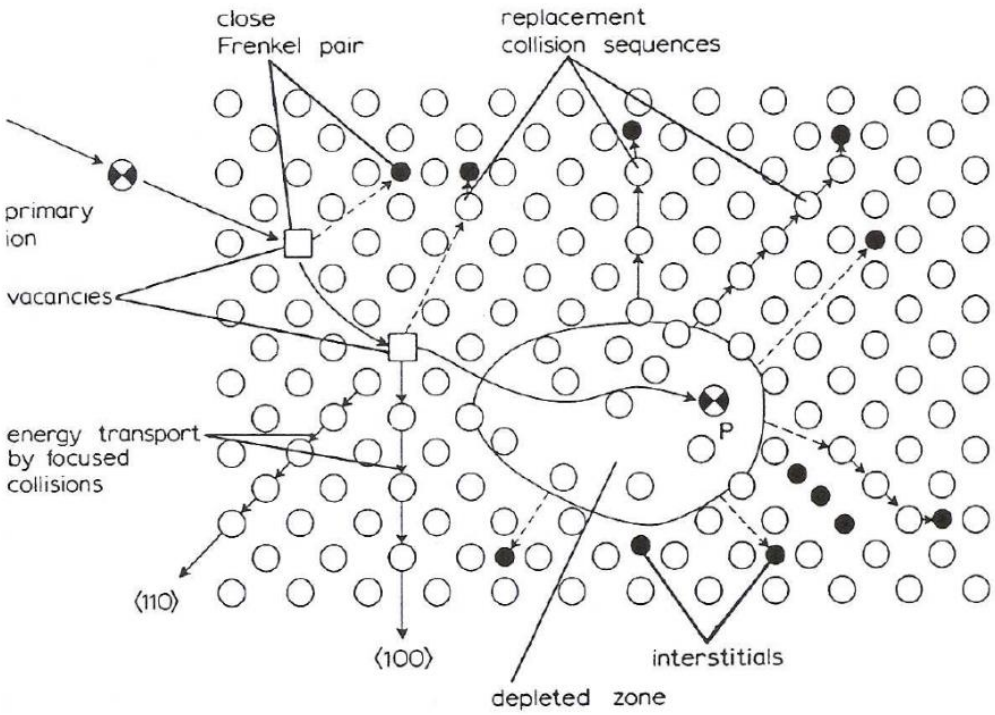

Figure 3.3: : A schematic representation of the collision cascade process showing the collision cascade and focused collision sequences extending beyond the main cascade regime [2].

3.4. Channeling

Channeling is when an incident ion is channeled down the spaces in the crystal structure and penetrates deeper into the target material than if it entered the crystal structure in a random direction. This process occurs when an ion moves at small angles to a row of atoms such that after each collision this angle decreases [43]. The present work used polycrystalline samples and any channeling effects is not considered.

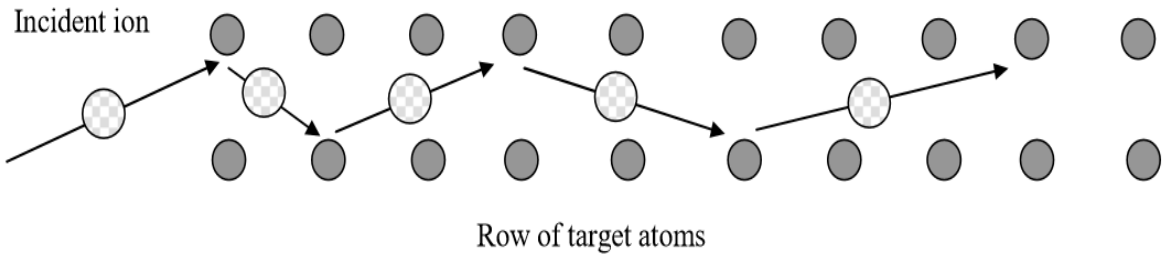

Figure 3.4: The channeling process in single crystals [43].

CHAPTER 4

4. EXPERIMENTAL METHODS

4.1. Introduction

This chapter gives a detailed description of the experimental arrangement and sample characterization procedures, including sample preparation. To achieve the goal of the experiment hexagonal boron nitride was chosen as a sample. Suitable ion beams, with different energies and fluences were selected.

4.2. Ion Implanter

A typical implantation system consists of a vacuum system, ion-source, acceleration column, mass-separator and target chamber (Figure 4.1)[44].

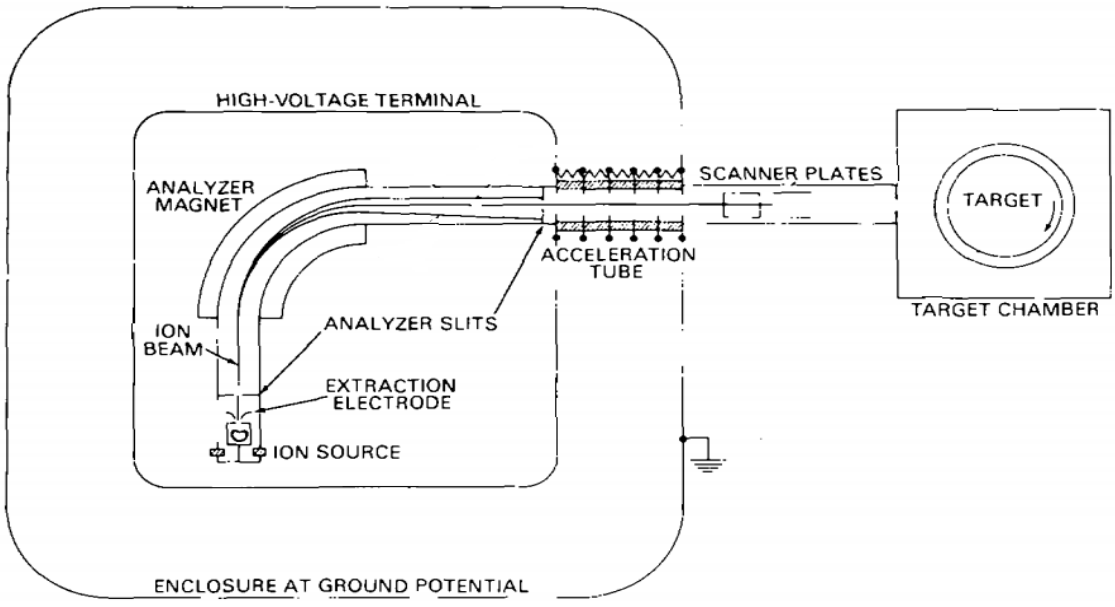

Figure 4.1: Schematic drawing of the 200-20A2F ion implantation system [45].

4.2.1. Vacuum System

High vacuum (10^{-5} to 10^{-7} Torr) is needed to reduce collision with some residual gases when ions are accelerated to the specimen. Thus, a pumping system is used to get the desirable pressure.

4.2.2. Ion sources

Gaseous material [helium, neon, lithium chloride (LiCl), or boron tri-Fluoride (BF_3)] is introduced into the ion-source (by a gas bottle or heating up lithium metal in carbon tetrachloride). Electrons are generated in the ion source by thermionic emission by passing a high current through a tungsten filament. These electrons collide with the gas molecules in the source chamber and this causes the valence shell electrons to be removed from the source chamber molecules to produce ions. An electron suppression electrode with a slit is biased with a negative potential relative to the filament; this causes positive ions to be attracted to the extraction slit and the positive ions are accelerated towards the analyzer magnet. The negative bias also serves to repel electrons back towards the filament.

The extraction electrode with negative bias pulls positive ions out of the ion-source and accelerates them to high energies before the analyser magnetic field can select the right type of ions. Some accelerated ions hit the extraction electrode surface, which generates X-rays and secondary electrons. The electron suppression electrode is needed to send electrons back into the source to increase the probability of the gas to be ionized and form positive ions. These electrodes have a narrow slit through which ions are extracted as a ray of ion flux forming an ion beam.

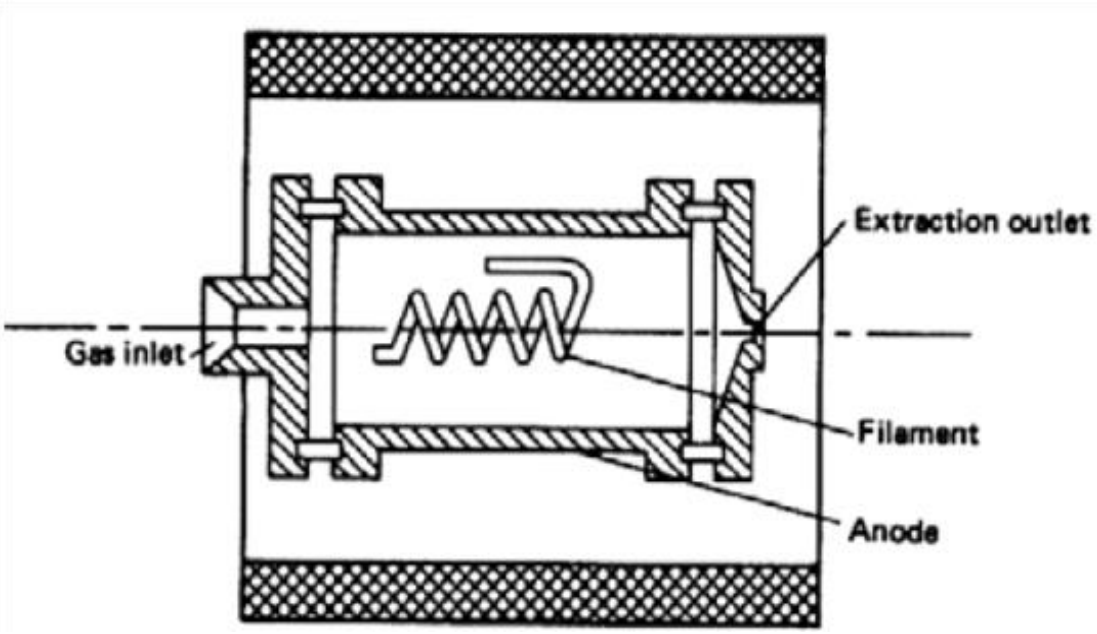

Figure 4.2: Schematic of the arc chamber of Freeman type ion source [46].

4.2.3. Mass analyser

Charged ions experience a force in a magnetic field (B). The positively charged particles have a velocity vector perpendicular to the magnetic field and the ions experience a force which is orthogonal to the ion velocity and magnetic field. The radius of curvature (R) for the path of ions with mass (m) and charge (q), moving with speed (v) perpendicular to the magnetic field is given by the following equation:

$$R = \frac{mv}{qB} \tag{4.1}$$

In this way, by adjusting the magnetic field, only selected ions with the mass that has the correct radius of curvature will enter the accelerating column. Ions with large and small, mass (m) to charge (q), m/q, will not pass through the beam tract at 90^{o}.

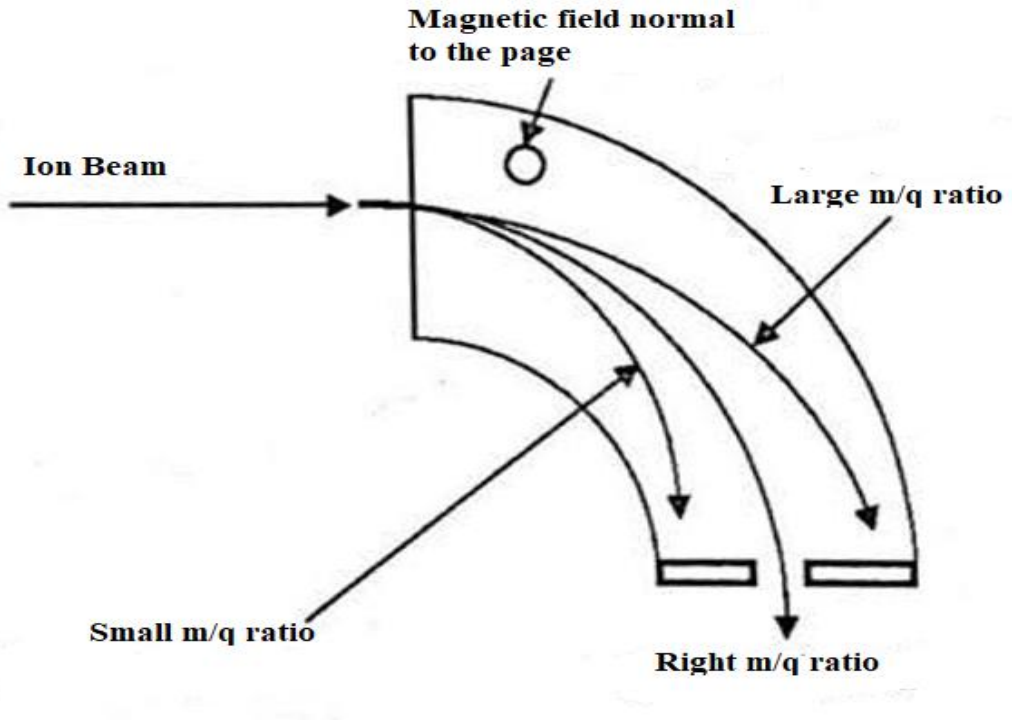

Figure 4.3: Mass analyser [46].

4.2.4. Acceleration column

The selected ions enter the acceleration column. These ions are further accelerated which gives them their final kinetic energy, which depends on the extraction electrode potential (V_{ext}) and acceleration electrode potential (V_{acc}, situated in the acceleration column). When doing high-energy ion implants various acceleration electrodes are connected in series along the beam line in order to accelerate the ions to ~100 kilo electron volts. For shallow ion implants the acceleration electrode is connected in reverse so that the ion beam is decelerated, this generates low energy ion beam[44].

4.2.5. Electrostatic deflection and neutral trap

A few ions before the desired implanted energy is achieved become neutralised during their passage through the vacuum. An electron exchange with atoms of residual gas causes ions to be neutralised before the desired implant energy is achieved. Neutrals are not desirable because they are not deflected by the scanner plates and can form a "hot spot" with extra fluence in the middle of the target sample [47]. To avoid this problem, parallel electrostatic deflection plates are used to deflect ions onto the specimen while neutrals will not be deflected. This function maybe included with one set of scanner plates.

There is an Electric field (E) between the x-axis and y-axis scanner (with opposite potentials). When a charged particle enters the plates, it will experience perpendicular forces due to the electric fields. Thus, this causes the desired ions to deflect. Neutrals will just pass through the plates without deflecting because they are not affected by electric fields. The x-y scan plates raster the ion beam over the surface of the specimen.

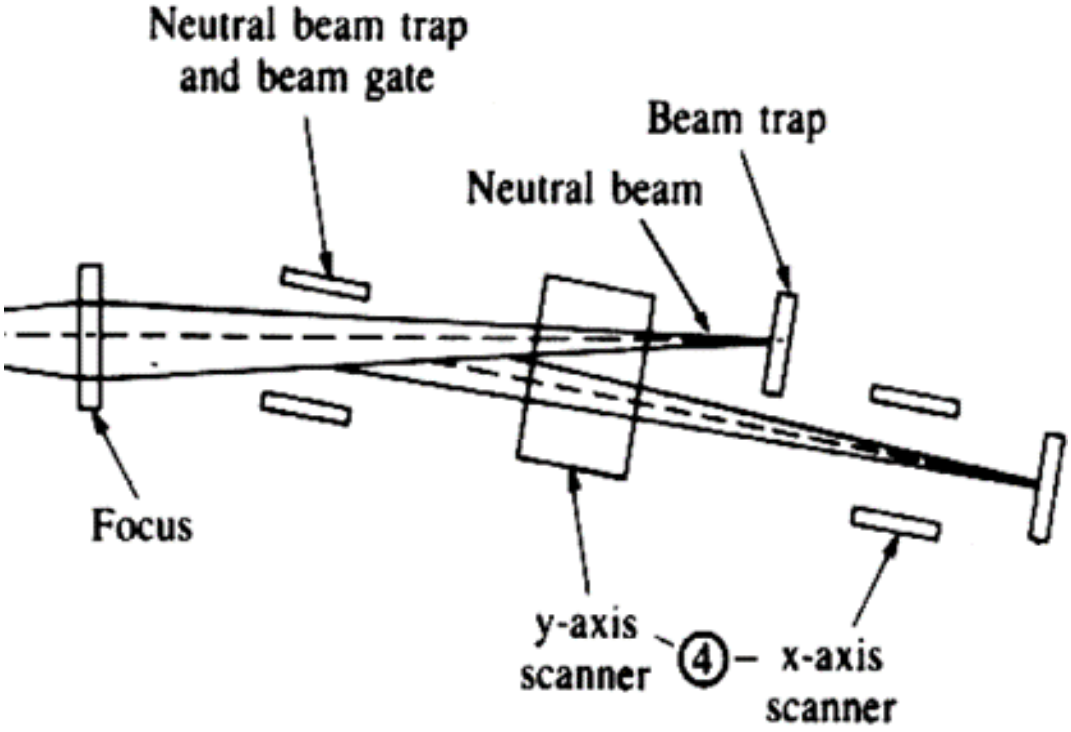

Figure 4.4: Diagram showing how the desired ions are separated from the neutrals [46] .

4.2.6. Faraday cup

A Faraday cup is an insulated block used to measure the ion beam charge. When the ions entering the cup have energies, higher than the work function of the cup material (i.e. stainless steel, carbon, graphite), this causes secondary electrons to be generated. The problem is that if a secondary electron leaves the cup this makes the charge on the cup look like an additional positive ion has entered. This problem can be solved by applying a positive bias potential around the Faraday cup.

4.3. Experimental procedure

4.3.1. Sample preparation

A hot pressed polycrystalline hexagonal boron nitride (h-BN) sample in the form of a rod (50 mm long and 15 mm in diameter) supplied by Good-fellow Cambridge Ltd (England), was used throughout this work (figure 4.5). A Well 3032 Model Diamond Wire saw located at the School of Physics, University of the Witwatersrand (Figure 4.6) was used to cut the samples into 2 mm thick slices before polishing the samples using a very fine sand paper (silicon carbide sandpaper 360- to 600-grit).

Figure 4.5: Hot pressed polycrystalline hexagonal boron nitride (h-BN) sample in the form of a rod.

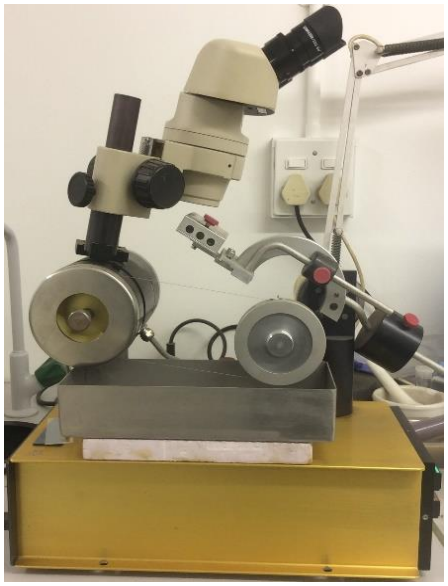

Figure 4.6: The 3032-model Diamond wire Saw.

The diamond saw cuts the samples using a very thin diamond wire of about 0.3 mm diameter. The wire keeps on rotating through a bath of water that has a lubricant used to keep it cool while cutting so that it does not break. A sample holder (figure 4.7) was designed to hold the sample while cutting, and a microscope attached to the Well 3032 is used for accurate measurement when cutting.

The Diamond Wire Saw was used to cut 2 mm samples. Twelve Samples were cut; four for room temperature, four for 150℃ and four for 300℃ implantations.

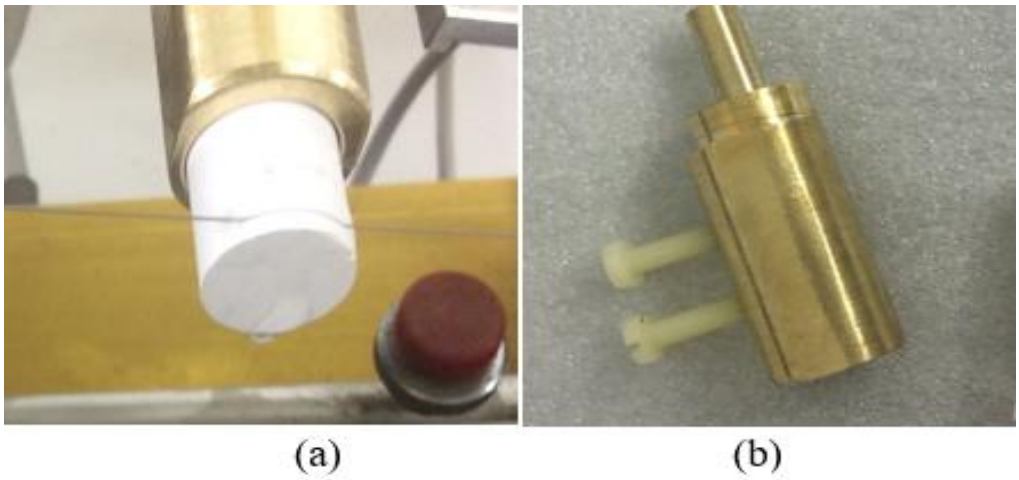

Figure 4.7: (a) Sample in sample holder, (b) Sample holder.

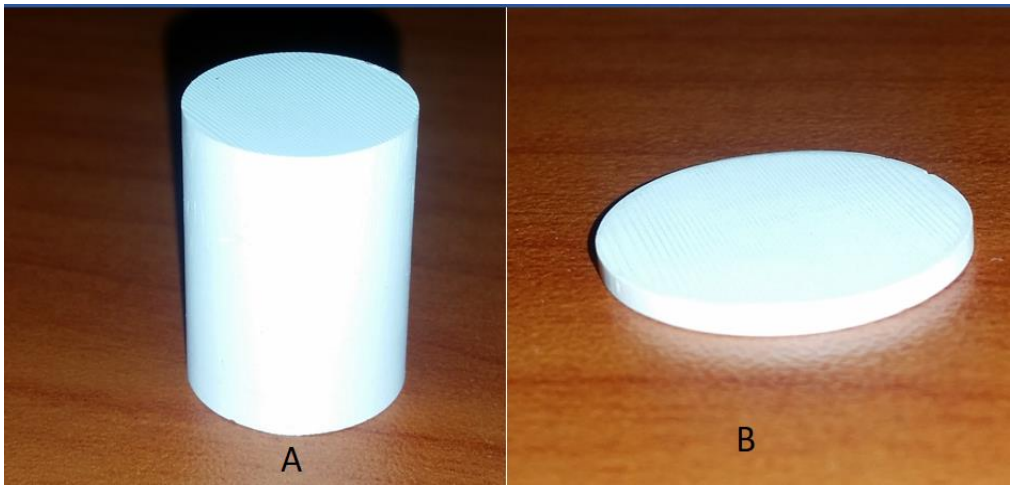

Figure 4.8: (A) h-BN sample in a form of a rod, (B) 2 mm sliced h-BN sample.

4.4. Radiation damage in boron nitride

4.4.1. Ion Implantation

The implantations were done using the 200-20A2F ion implanter at iThemba LABS Gauteng, South Africa. For these measurements, the same ions implanted in previous studies were used with the addition of Ne^{+} as a check on possible chemical effects. A sliding shutter, operable from outside the vacuum chamber, was used so that all the fluences for each set conditions could be implanted in one run, in a set of parallel strips, for direct comparison.

The polished h-BN samples were mounted on the implanter sample holder end station where they were implanted with desired ions (i.e helium, lithium, boron and neon). Boron, helium and neon ions were generated from Boron tri-fluoride (BF_3), helium and neon gas, respectively, while lithium ions were generated by reacting the lithium metal with carbon tetrachloride (CCl_4). Ionization took place in the ion source chamber of the implanter generating plasma. The specific ions were then selected by the mass analyzer in terms of their mass to charge ratios *m/q* and accelerated at the energy of choice (150 keV, was used throughout the experiments). The accelerated ions were then implanted into the h-BN sample at a specific fluence ($ions/cm^2$), and the implantation current monitored by the Faraday cup.

Figure 4.9: The Varian-Extrion 200-20A2F Ion implanter located at iThemba LABS (Gauteng), South Africa.

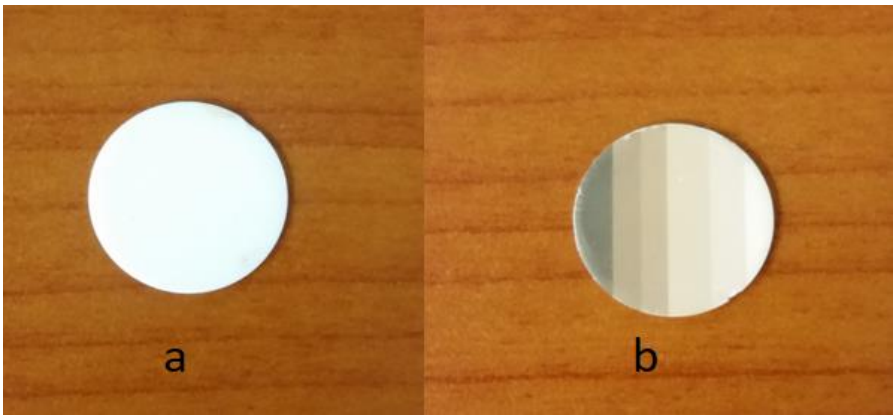

Figure 4.10: a) h-BN 2mm slice before implantation, and (b) after implantation.

All implantations were carried out at energy 150 keV. The implantations were done on parallel strips, for direct comparison, with each strip implanted at a different fluence and the higher the fluence the darker the strip colour (e.g. the entire surface was implanted with a fluence of $1x10^{14}$ ions/cm^2. The travelling mask was used to only cover 3mm of surface; and an additional fluence $4x10^{14}$ ions/cm^2 was implanted

on the exposed area of the sample to make $5x10^{14}$. The mask was moved down a further 3mm and an additional $5x10^{14}$ ions/cm^2 was implanted and so on to make $1x10^{15}$ ions/cm^2)as shown in figure 4.10.

4.4.2. Stopping and Range of Ions in Matter (SRIM®) simulations:

SRIM-2013 was used to determine the depth distribution and collision details of implanted ions. The simulations were done at 150 keV for ions used (Helium, He^+, Lithium, Li^+, Boron, B^+, Neon, Ne^+), implanted into h-BN with a density of $2.27 g/cm^3$.

4.5. Characterization

Raman spectroscopy and X-ray diffraction (XRD) techniques were used to characterize the h-BN samples to confirm a cubic-BN induced phase transformation. This was done by taking measurements on the samples before and after implantation.

4.5.1. Raman spectroscopy

Raman spectroscopy was used to analyze the samples to confirm any ion induced phase change reported in References [3], [4], [2], [5]. This was done by taking Raman measurements of the h-BN samples before and after implantation.

Raman spectroscopy is a characterization technique based on analyzing the Raman scattered light. When a material is illuminated with monochromatic radiation (i.e. laser light) some light is transmitted, absorbed and some light will be scattered after its interaction with the vibrations related to the molecular bonds of the material. In Raman spectroscopy a photon scatters of a phonon (lattice vibration). When electrons relax after absorbing incident radiation and release a photon, this is termed photoluminescence. If the scattered radiation has frequency that is equal to the frequency of the incident radiation, this constitutes Rayleigh scattering (when an

excited electron relaxes and returns to the same vibrational state from which it started). This means there is no change in frequency, known as elastic scattering. When scattered radiation has a frequency different to the frequency of incident radiation, it constitutes Raman scattering. The Raman scattering process where the electron in the ground vibrational state is excited to a virtual state then relaxes to an energy state that is higher than the ground state is called Stokes scattering. When an electron begins in a vibrational state that is higher in energy than the ground state and is excited to a virtual state then relaxes to the ground state that is less in energy than when it started is called anti-Stokes scattering. This change is frequency is known as inelastic scattering.

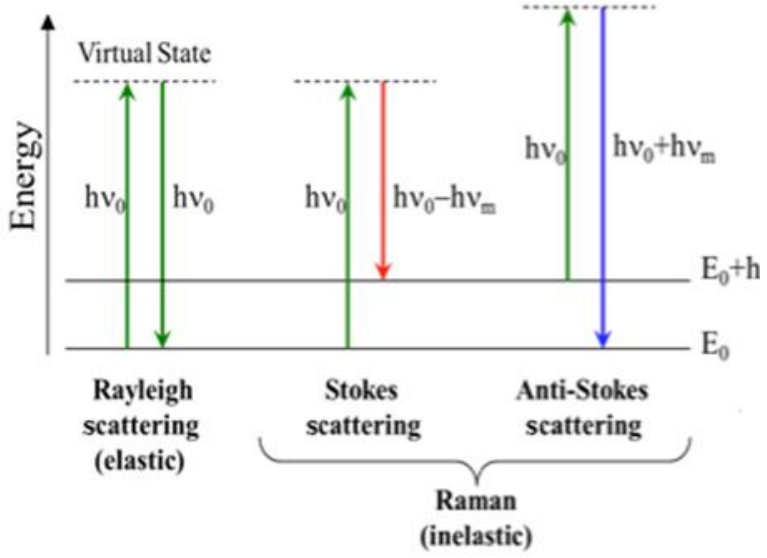

Figure 4.11: An illustration of the Rayleigh and Raman scattering process (Stokes and anti-Stokes).

Raman instrumentation:

Measurements were done using the Jobin-Yvon T64000 Raman spectrometer at the School of Physics, University of the Witwatersrand. An intense Coherent 514.5nm Argon (Ar^{+}) laser beam source was used to perform the Raman excitation. A laser transmission filter is used to narrow the incident beam linewidth because lasers are not perfectly monochromatic light sources. However, if useful data is to be obtained from the signal components, it is therefore necessary for careful signal processing because Raman scattered light is very weak and is very close to Rayleigh scattered light which is several orders of magnitude stronger [1],[2]. The spectrometer is a triple mono-chromator dispersive system. The filtered beam is narrowed down to a volume of about $1\mu m^3$ on the sample using a set of objective lenses. A holographic notch filter between the sample and monochromators is used to reject unwanted light before the Raman signal can be detected and measured by the spectrometer.

The filtered light is directed to the monochromators, they separate a broadband signal into single spectral lines according to wavelengths and they are based on diffraction grating dispersive systems. If the Raman signal is not so close to the Rayleigh line, the Jobin-Yvon T64000 spectrometer can be used in single spectrograph mode without compromising the resolution. Charge-coupled device (CCD) detectors, built onto the exit slit of the third monochromator, detect and convert detected photons to digital signals that can be stored to a computer as data.

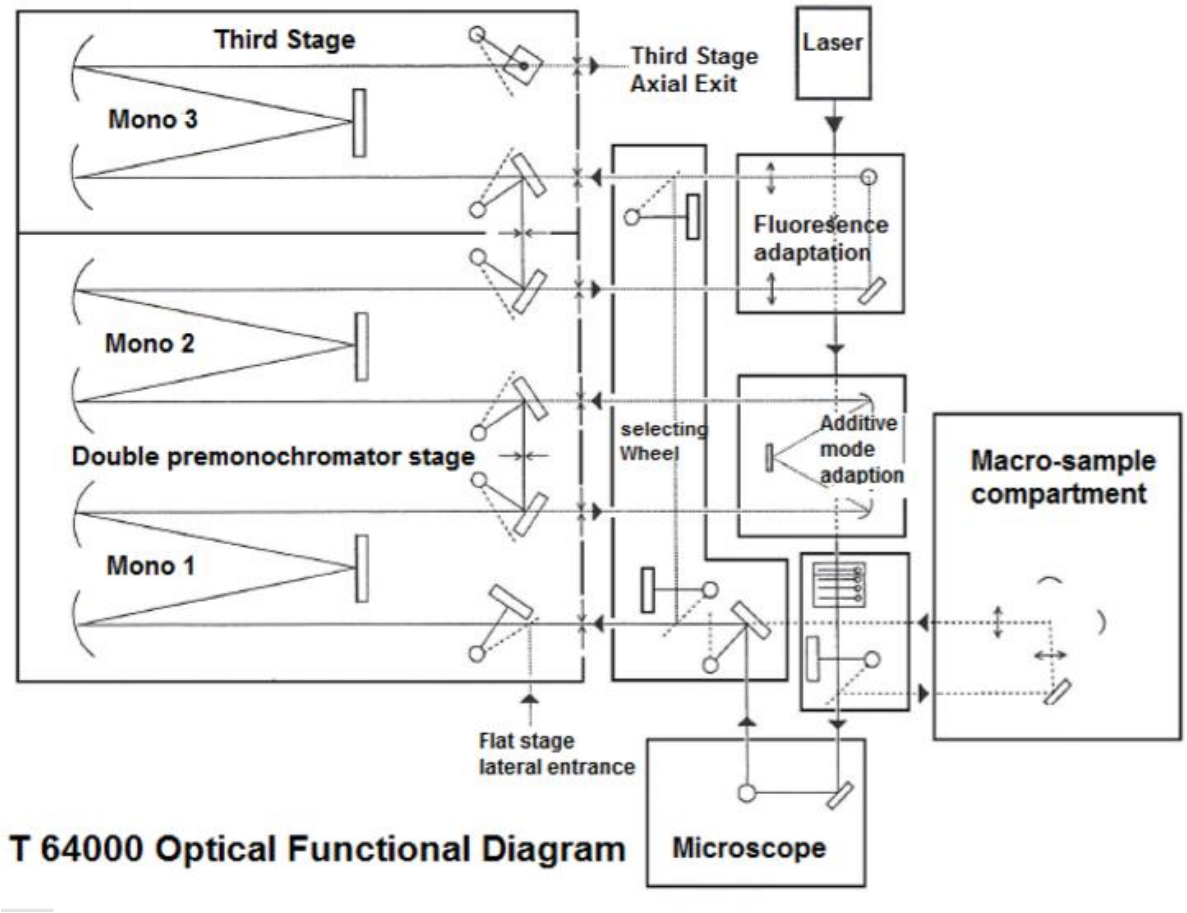

Figure 4.12: Schematic diagram of the Raman Spectrograph showing the beam path(From the Instruction Manual for the Jobin-Yvon T64000 Raman Spectrograph]) [2].

4.5.2. Experimental detail

The Raman spectrometer is controlled by a computer. The spectrometer can be operated in macro (measurements are done in a macro compartment for very large sample specimen) or micro-Raman mode (measurements are done in a microscope stage). The laser light can be narrowed down to 1µm on the sample surface. When the measurements are carried out on the X-Y microscope stage the spectrometer is operating in 2-D mapping mode, and with the aid of piezo Z-stage scanner, it is possible to operate the spectrograph in a 3-D mapping mode. For experimental work in this dissertation, the micro-Raman mode was used.

The measurements were done under ambient conditions, using a 514 nm argon laser as an excitation source, with the beam power at 200mW. An 1800 grooves/mm grating in the spectrometer and a nitrogen cooled CCD detector were part of the system.

4.5.3. Hardness testing

Hardness is a key property of materials. The stiffness of a material can be determined depending on the hardness test technique used, but for the purpose of this experiment, indentation measurements were carried out. These measurements can be performed on a macroscopic or microscopic scale. Macro-indentation refers to tests with applied load of more than 1kg, and micro-indentation is with applied load of less than 1kg. In this instance, the hardness can be determined by measuring the depth of indentation or the area caused by a specific indenter on the tested material (i.e. hardness is determined by the dent created when forcing a specific indenter into the test material under a specific load (F) for a given time) .

A deeper indentation indicates less resistance to plastic deformation of the tested material (when the material is soft, the depth of penetration is great) resulting in lower hardness value. Therefore, the results help to assist in material selection (i.e., materials suitable for cutting tools or those with high wear resistances).

Indentation techniques are selected based on the specimen dimensions, type of materials and the required hardness information.

In this experiment, the Vickers hardness test was used. The concept of the technique is explained as follows: A diamond pyramid indenter (with an included angle of 136°, as shown in figure 4.13) was used for this hardness test. This method is also known as diamond hardness test (DPH) due to the indenter shape. The diamond indenter is pressed on the surface of the specimen to produce a square based pyramid. Due to the angle (ϕ=136°) caused by the applied load (F) between the opposite faces, this makes it simple to derive the required hardness equation. Thus, the Vickers hardness value (VHN)[10] is calculated from the applied load divided by the area (A), and the following equation is obtained:

$$\mathrm{VHN} = \frac{F}{A} = \frac{2F\sin\left(\frac{\emptyset}{2}\right)}{d^2} = \frac{1.8544F}{d^2}, \qquad (4.2)$$

where d, is the average length of the diagonals = $(d_1+d_2)/2$

[10] For derivation of the hardness equation, refer to Appendix at the end of the dissertation.

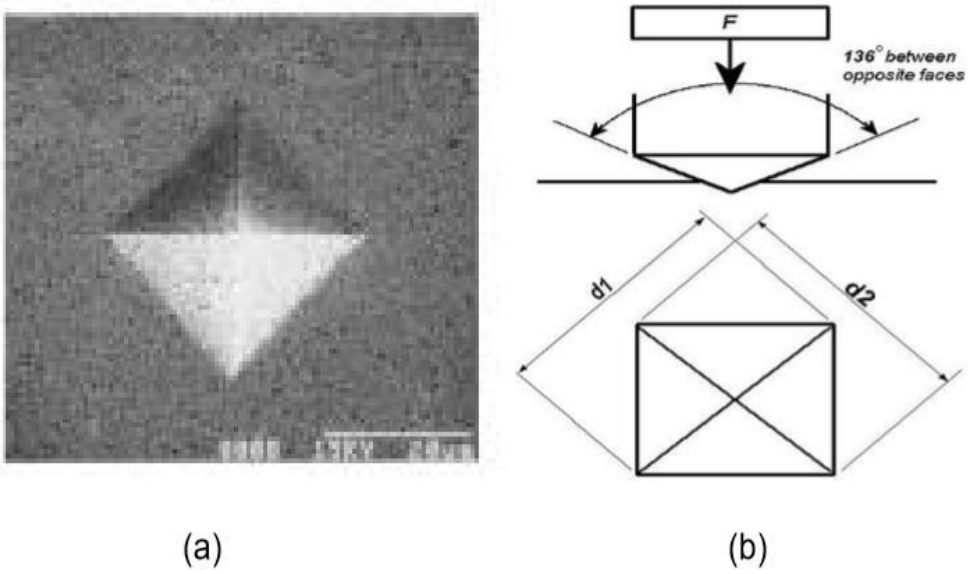

Figure 4.13: (a) SEM image of indentation, (b) Diagram showing diagonals of the indentation on the surface of the material after removal of the load [48].

4.5.4. X-ray diffraction

X-ray diffraction is a technique used for the study of crystal structures and atomic spacing. It is based on constructive interference of monochromatic X-rays generated by a cathode ray tube. A tungsten filament (cathode) is heated by passing a current through it, this causes electrons to be emitted towards a metal target (anode) (e.g. Cu or Mo), Figure 4.14. The electrons will strike the target metal and excite electrons from the core-level. Electrons in higher levels will drop down into the vacancies in the core level, releasing energy in the form of X-rays called characteristic X-rays (K_α and K_β X-rays)[11]. Bremsstrahlung X-rays are formed when incident electrons are deflected in the core level thus losing energy and emitting broad-spectrum X-rays. These X-rays are filtered out and the monochromatic –X-rays are then directed towards the sample. The interaction of the incident rays with the sample produces constructive interference (and diffracted X-rays) when conditions satisfy Bragg's law. By scanning the sample through angles from 0 - 2θ all possible diffracted X-

[11] The K_α Cu X-rays have wavelength of ~0.15nm and K_β ~0.13nm. The reason why X-rays of the wavelength ~0.15 nm is needed and ~0.13nm X-rays are filtered, is that to see the interference patterns observed at the specific diffracting angles for the crystal; K_α X-rays have much higher intensity and would give a very good signal to noise and more importantly the wavelength of the X-rays must be comparable to the crystal spacing, for large diffraction angles (e.g. 0.15nm is good)

rays would be detected (Figure 4.15) and a diffraction spectrum of the sample obtained.

Every diffraction peak is unique; it determines the *d*-spacing of the scattering set of planes. The material's atomic composition, arrangement, and crystallite orientation information are obtained from the peak position, intensity and width of the diffraction peaks. The information about the spacing of lattice planes in the crystal structure is provided by the diffraction peak positions. In this dissertation, grazing incidence X-ray diffraction (GIXRD) was used.

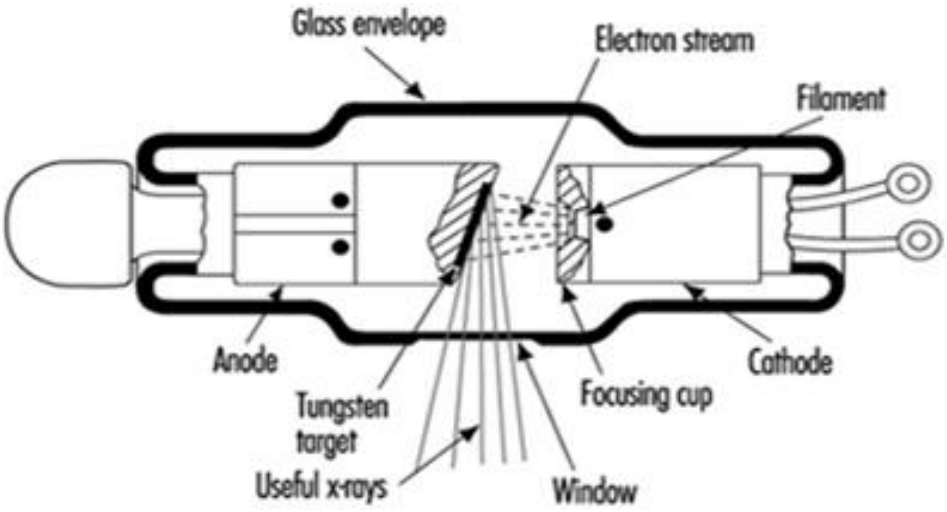

Figure 4.14: X-ray generator [49].

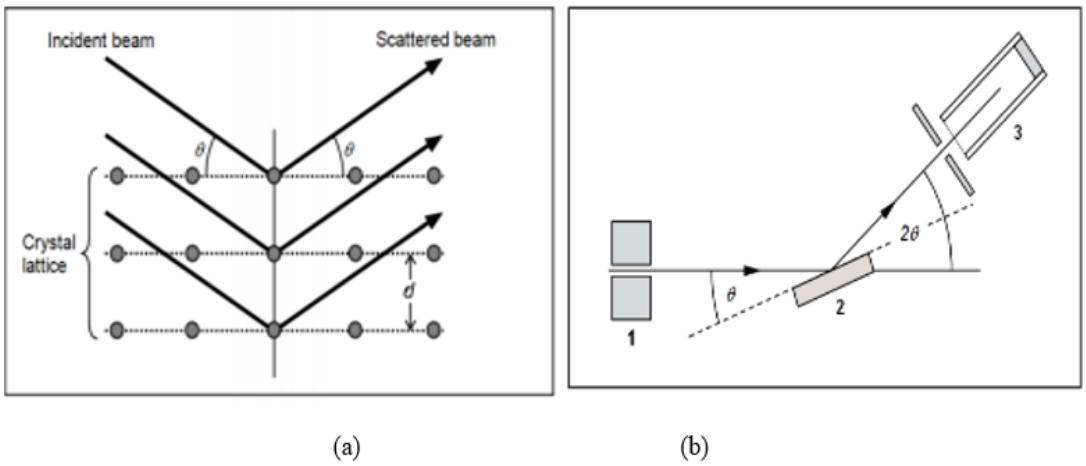

Figure 4.15: (a) Reflection of x-rays at lattice planes, (b) the principle of X-ray diffraction [49].

Glancing Incidence X-ray Diffraction (GIXRD)

GIXRD is a technique used to characterize and study crystal sub-surface structures, unlike conventional XRD that gives data about the bulk structure of a material. The incident X-rays arrive at a glancing angle (w) with respect to the surface of the sample. When the incident glancing angle (w_i) is larger than the critical angle (w_c), for reflection ($w_i > w_c$), the reflected X-rays will be able to reveal the sub-surface information of the material.

The measurements were done on the hBN sample before and after implantation, using the D8 ADVANCED Bruker X-ray diffractometer located at the school of Chemistry, University of the Witwatersrand. The diffractometer is equipped with CuK_α radiation of λ=1.504Å, voltage of 40kV and 40mA current.

CHAPTER 5

5. RESULTS AND DISCUSSION

5.1. Stopping and Range of Ions in Matter (SRIM)-2013 Simulation

SRIM-2013 version was used to determine the depth distribution (range of the implanted ions) and the simulated radiation damage profile of the vacancies created by the implanted ions in its collision cascade. The simulations were done at 150 keV for ions used for implantation (He^+, Li^+, B^+, Ne^+). This information was used to determine the simulated damage density and range of the implanted ions.

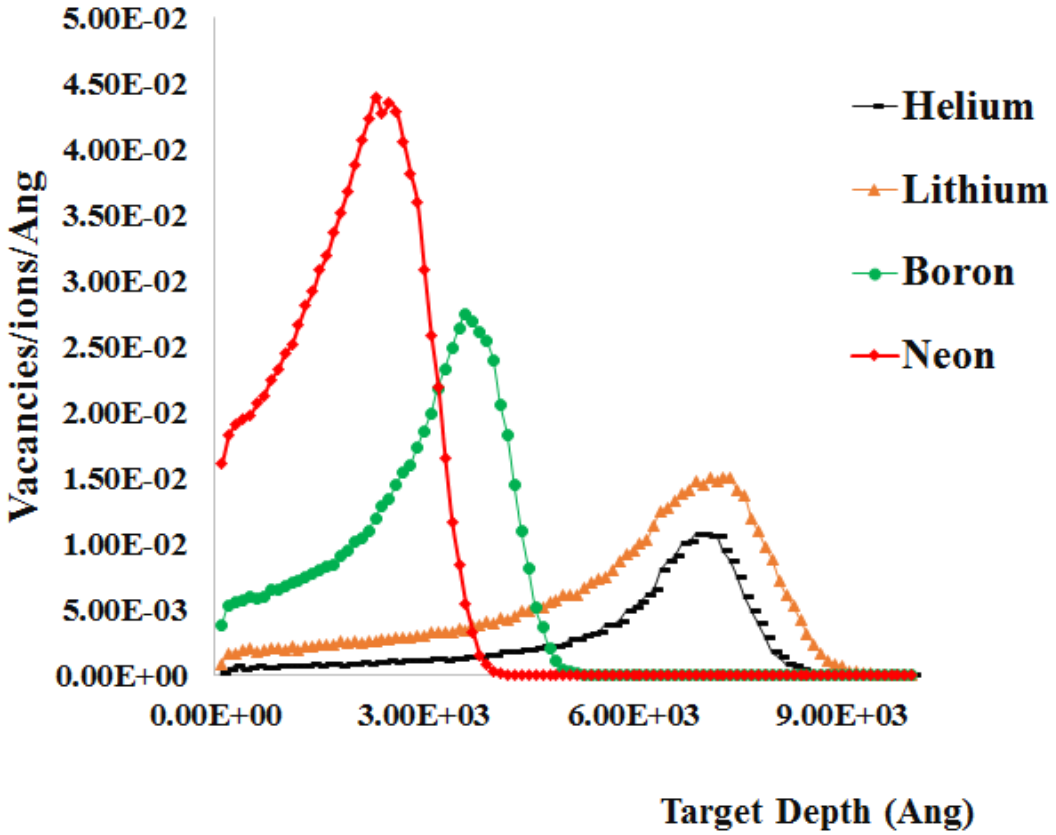

Figure 5.1: SRIM simulation for the number of vacancies per ion and unit length (Å) versus depth for boron, lithium, helium and neon ions implanted into h-BN at 150 keV. The similarities of He^+ and Li^+ depths have been confirmed.

Fig. 5.1 above shows that neon and boron ions cause more damage in the h-BN sample as compared to helium and lithium. Neon (Ne^+) and boron (B^+) produced $4.39x10^{-2}$ vacancies/Å at a depth of $2.40x10^3$ Å and $2.75x10^{-2}$ vacancies/Å at a depth of $3.70x10^3$Å respectively, while helium (He^+) and lithium (Li^+) produced $1.06x10^{-2}$ vacancies/Å at depth $7.10x10^3$ Å and $1.40x10^{-2}$ vacancies/Å at $7.50x10^3$ Å, respectively. Therefore, heavier ions penetrate less into the surface but cause more damage. Lighter ions penetrate deeper into the surface but causing less damage for the same fluence.

.

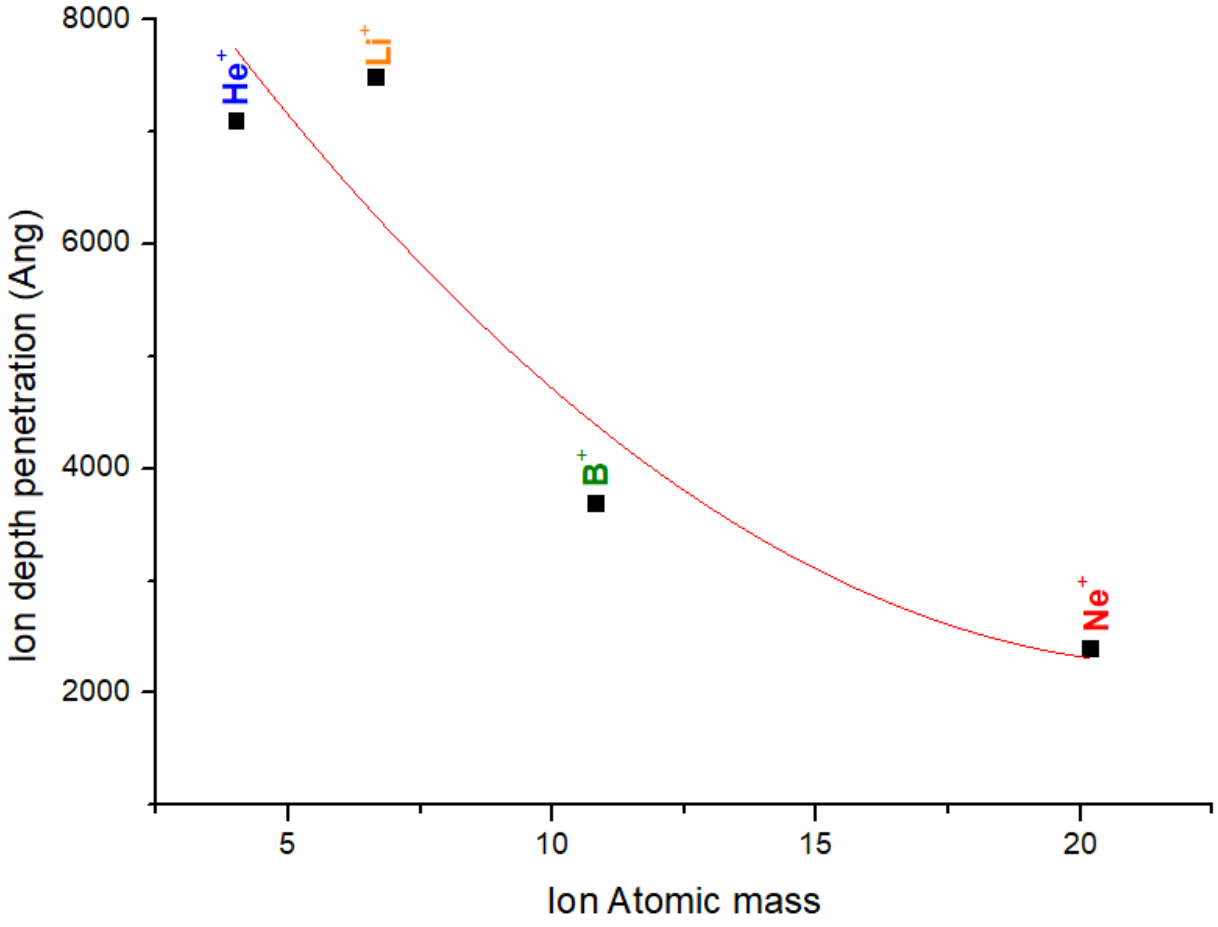

Figure 5.2: Atomic mass of various ions used as a function of Ion penetration**.**

Fig. 5.2 shows ion penetration depth as a function of atomic mass. An increase in atomic mass gives lower penetration depth, confirming that heavier ions penetrate less into the surface of h-BN.

5.2. Raman spectroscopy results

Micro-Raman spectroscopy was used to analyze the samples and confirm any ion induced phase change, by taking measurements before and after implantation using a Jobin-Yvon T64000 Raman spectrometer at room temperature. The Raman spectra results presented here are only for helium and neon at room temperature implantations and one for the un-implanted h-BN sample. Previously taken Raman spectra for boron and lithium at room temperature implants are presented in detail in by Aradi et.al [5], Figs. 5.6 and 5.7.

The h-BN Raman spectra are shown in Figs. 5.3 to Fig. 5.5 below, where Fig. 5.3 is for virgin h-BN, which displays the intense vibrational mode at 1367 cm^{-1} due to the sp^2 hybridized BN planar bonding. This peak decreases in intensity with increasing fluence, thus, it is evident that there is some radiation damage to the h-BN sample.

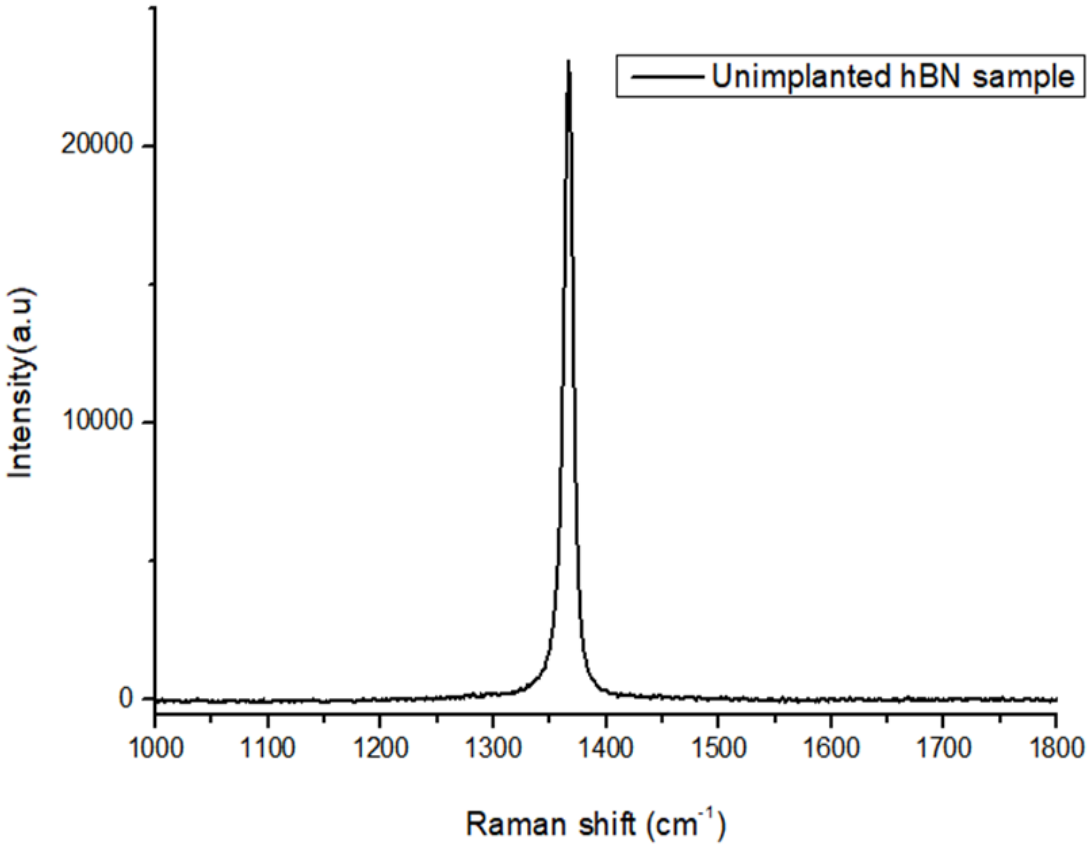

Figure 5.3: Unimplanted h-BN Raman Spectrum

The Raman signal for large single crystal c-BN shows two vibrational modes, the translational optical (TO) mode at 1056 cm^{-1} and longitudinal optical (LO) phonon mode at 1305 cm^{-1}. Cubic BN with nanoscale particles tends to show the LO phonon modes, shifted to lower energies, as we see here after implantation as broad peaks around 1300 cm^{-1}. This peak indicates a phase change to cubic-BN, as reported in detail before [3, 4, 5, 6].

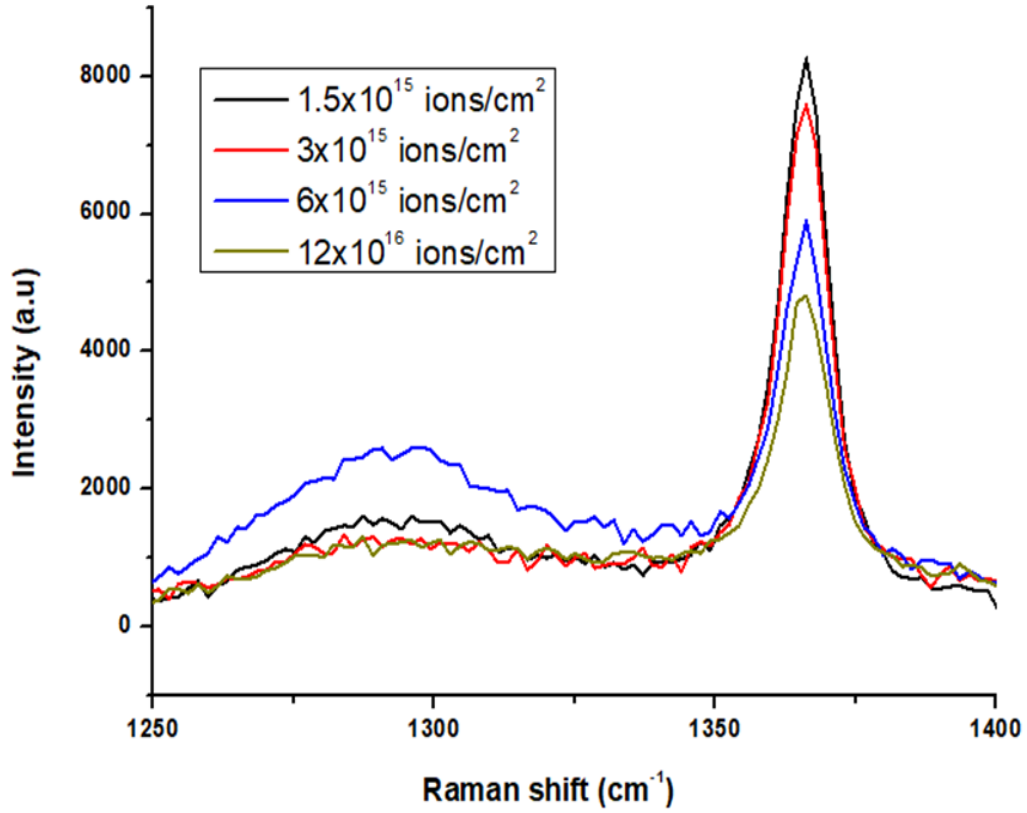

Figure 5.4: Raman spectra of h-BN samples implanted with helium ions (He^+).

The present results mirror those of previous work, showing an optimum ion fluence followed by a decrease with accompanying radiation damage, confirming a phase change to nano-cBN in the implanted layer of a few 100 nm.

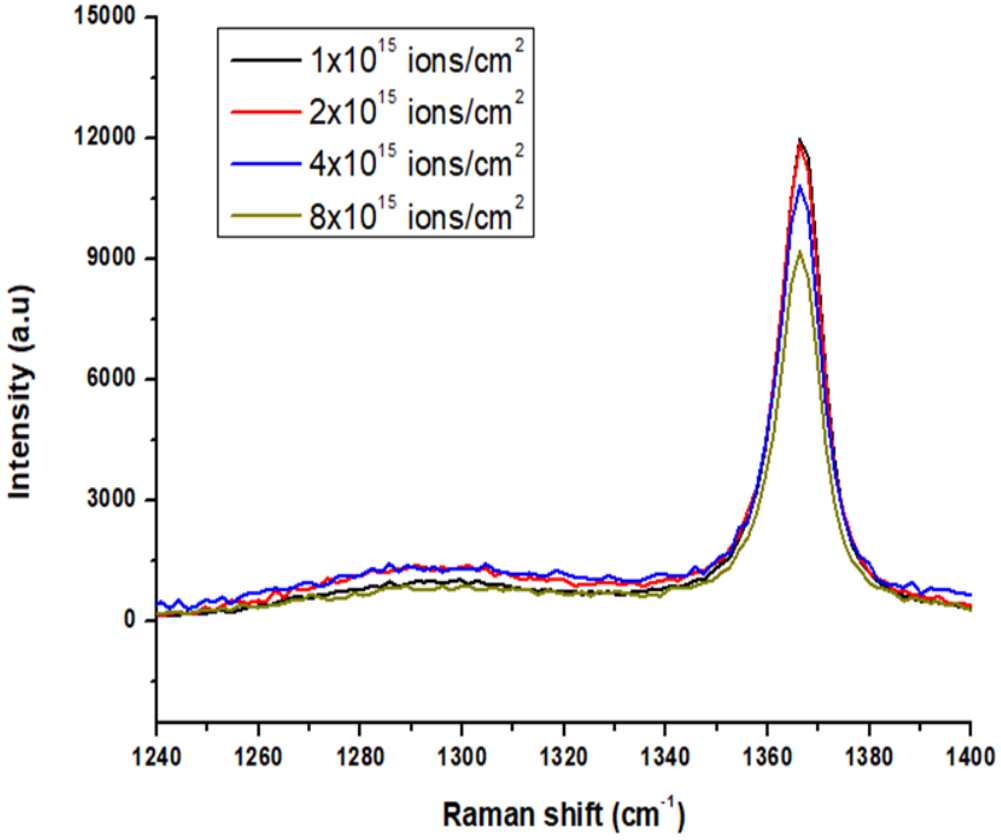

Figure 5.5: Raman spectra of h-BN samples implanted with neon ions (Ne^{+}).

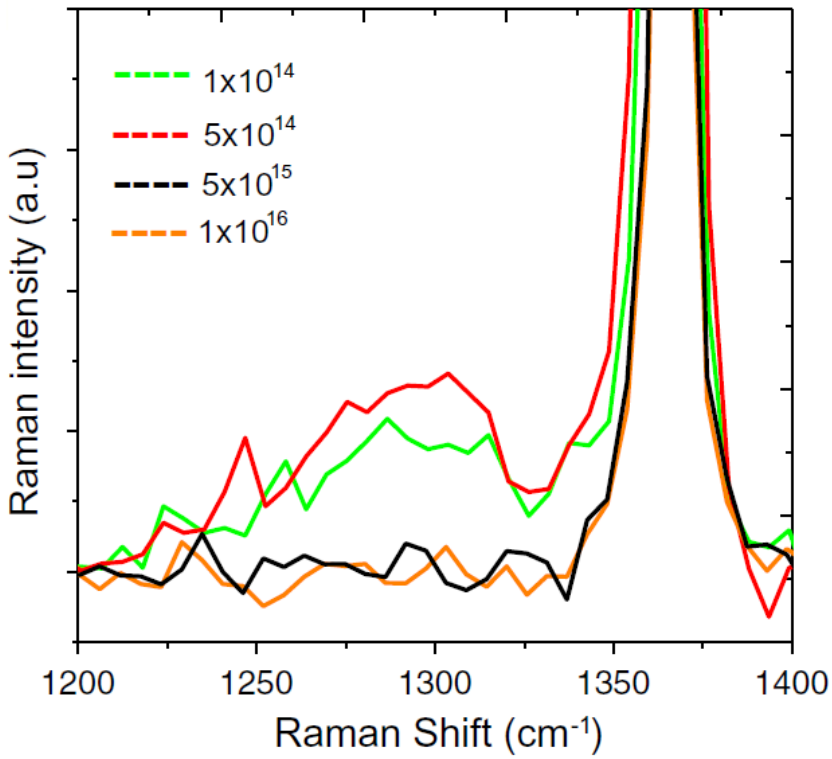

Figure 5.6: Raman spectra of h-BN samples implanted with boron ions (B^+) [5].

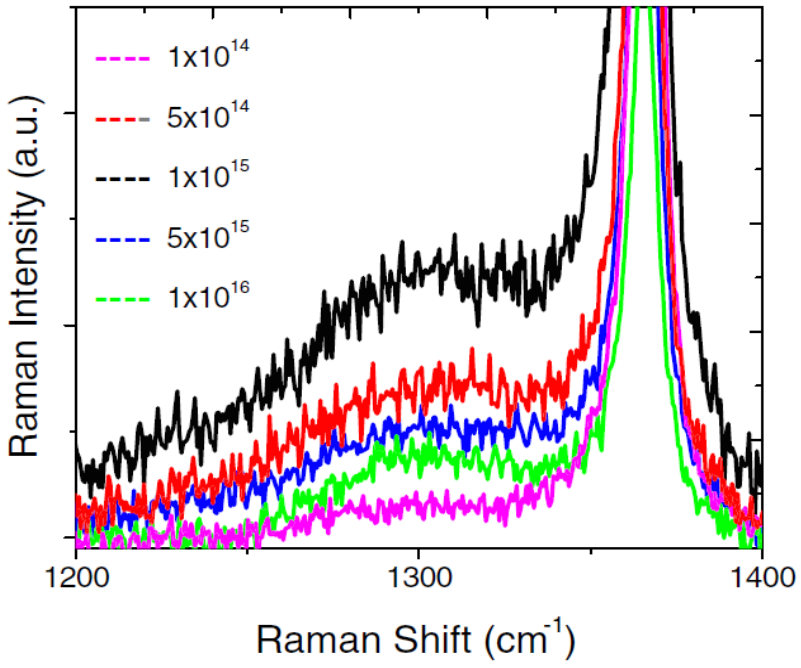

Figure 5.7 Raman spectra of h-BN samples implanted with lithium ions (Li^+) [5].

5.3. Micro indentation

5.3.1. Varying fluence at room temperature

The implantations for these samples were done by varying the ion fluence at room temperature, and then hardness micro-indentation measurements were taken. The first set of hardness measurements was taken on the un-implanted samples with the indentation load of 100g and the overall average hardness measurement of the as-grown h-BN was 13.4 ± 2 kg/mm^2.

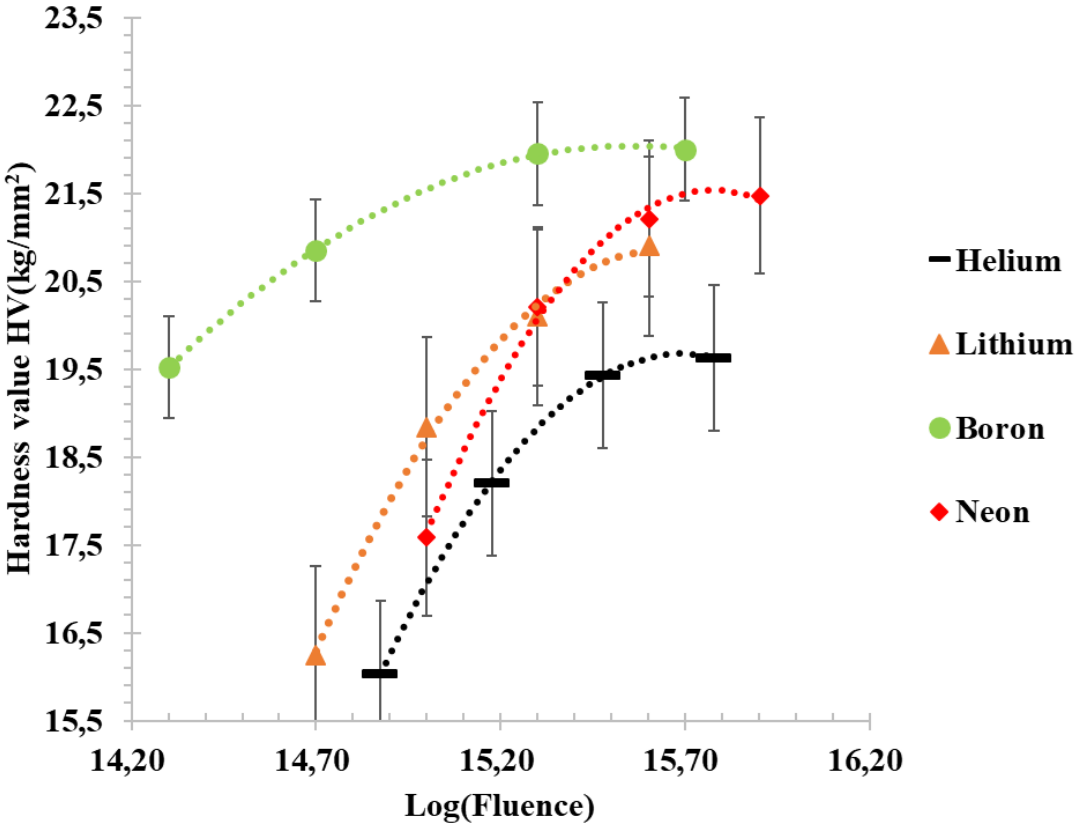

Figure 5.8: Hardness as a function of logarithmic fluence.

The micro-indentation curves in Fig. 5.8 show a trend, that is, for each ion beam implanted into h-BN there is an optimum hardness value. Samples implanted with helium and lithium gave 19.63 kg/mm^2 and 20.90 kgmm^2 optimum hardness values,

respectively. Boron and neon implanted samples gave 22.00 kg/mm^2 and 21.34 kg/mm^2, respectively.

From the obtained optimum values, heavy ions caused the implanted region on the sample to increase in hardness compared to the light ones. However, what is surprising is that boron ions caused more hardness compared to neon even though neon caused more damage.

The damage density for heavier ions (B^+ and Ne^+) is closer to the surface, about 550 nm and 450 nm respectively, while for light ions (He^+ and Li^+) it lies much deeper, about 600 nm for the same fluence. The damage density from TRIM simulation suggests that the damage that is close to the surface is caused by heavier ions because they slow down much faster as they are moving slower when they enter the hBN sample, thus the induced hard phase is close to the surface of the material. The Vickers hardness test measurements for He^+ and Li^+ ions show that the damage density lies deeper and thus the materials has a softer surface, which is still primarily hBN. This could possibly be explained by asking the following question. What is the dominant process between nuclear and electronic stopping for the various implanted ions? The research by Aradi et.al. [1] shows that electronic stopping dominates for light ions, thus, this could have a chemical effect on the sample and nuclear stopping dominates for heavy ions. In the case of neon and boron ions, nuclear stopping is dominant because atoms are being knocked off from their positions. While for the sample implanted with helium and lithium ions, electronic stopping is dominant and produces a chemical effect, causing some damage deeper into the sample [40].

5.3.2. Varying temperature at constant fluence

The micro-indentation hardness results are presented together in Figs. 5.9, 5.10 and 5.11. The implants were done at room temperature, 150 °C and 300 °C at the same ion fluences with the same ions and energy.

The maxima in the curves are quite pronounced, especially when plotted logarithmically, showing that there is a clear increase in hardness value over the unimplanted sample, with an optimum fluence followed by a decrease depending on the fitted curves. There is a trend with ion mass, except for Ne^+.

This is a possible confirmation that some of the h-BN is structurally deformed to c-BN. There is an optimum level of radiation damage for this. Slightly higher hardness levels are obtained with the heavier ions; but Ne^+ ions do not fit well with this trend.

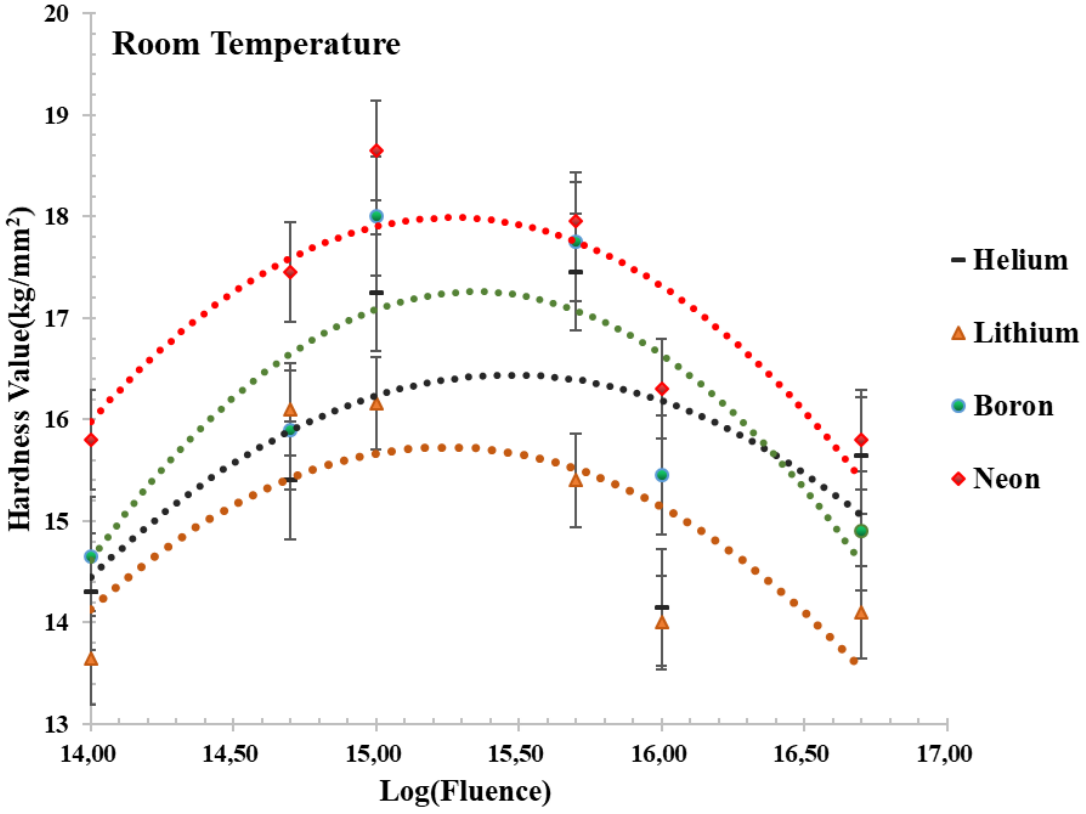

Figure 5.9: Hardness as a function of logarithmic fluence for all h-BN samples implanted with He^+, Li^+, B^+ and Ne^+ ions at 150 keV and room temperature.

The 150 °C implants gave comparable results but higher Vickers hardness values compared to 300 °C and room temperature implants. The room temperature sample implanted with Ne^+ ions has a higher hardness value than 150 °C and 300 °C Ne^+ implants. This could be that implanting at 150 °C and 300 °C is like annealing the sample and restoring some of the damage which would otherwise promote the h-c phase change.

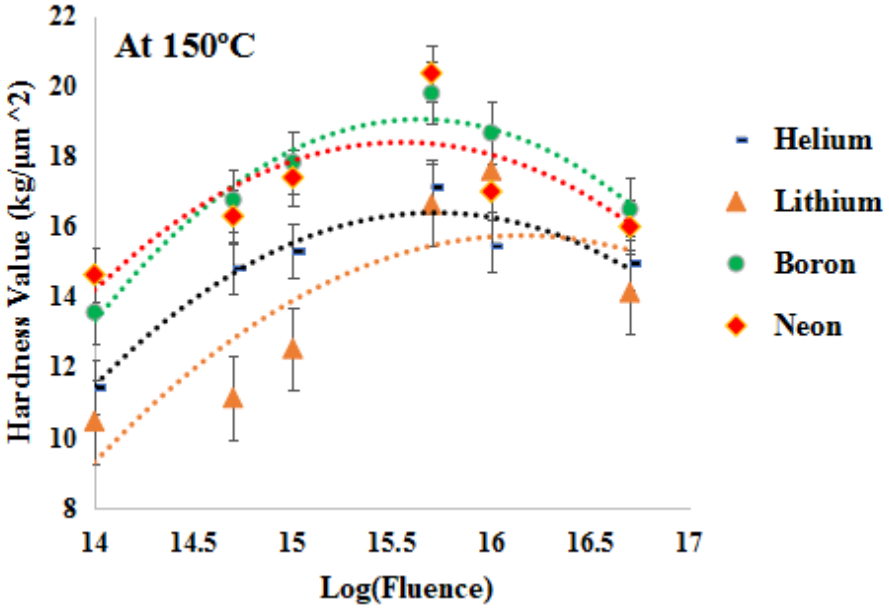

Figure 5.10: Hardness value as a function of logarithmic fluence at 150 keV and a measured temperature of 150 °C.

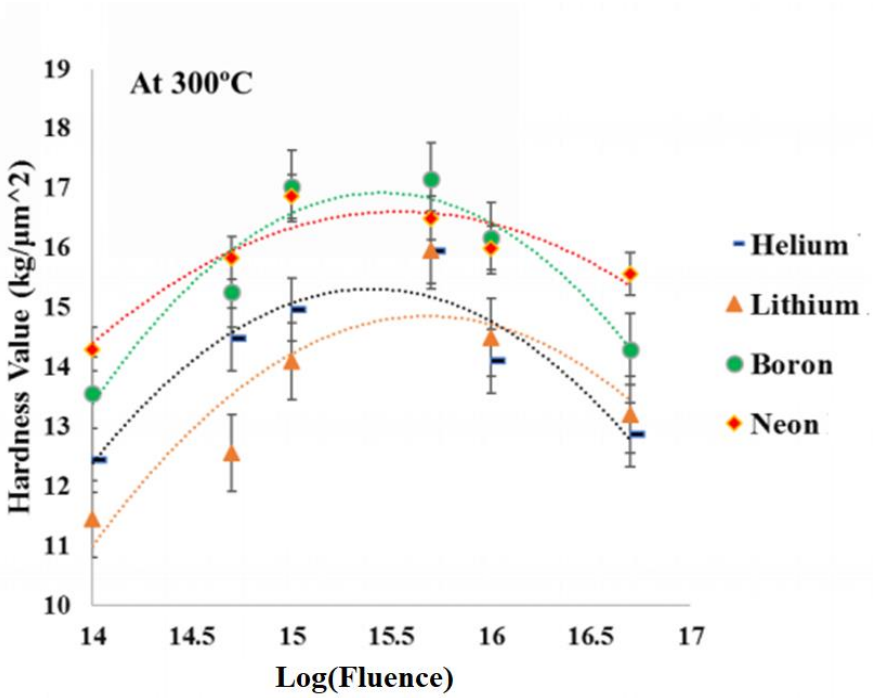

Figure 5.11: Hardness value as a function of logarithmic fluence at 150 keV and a measured temperature of 300 °C.

A comparison of the optimum fluences at room temperature determined by Raman spectroscopy and by indentation testing is important and is shown in Table 5.1. The values are similar, considering the errors inherent in ion implantation experiments. The optimum indentation values tend to be higher than the Raman values, possibly because the radiation damage itself may increase hardness.

Table 5.1: Optimum fluences determined by Raman spectroscopy and by indentation testing at room temperature (Units are 10^{15} ions/cm^2).

Ions:	Helium (He^+)	Lithium (Li^+)	Boron (B^+)	Neon (Ne^+)
Raman	6.0 ± 0.2	1.0 ± 0.2	0.5 ± 0.4	4.0 ± 0.1
Indentation	4.8 ± 0.4	3.9 ± 0.5	3.5 ± 0.5	5.5 ± 0.4

5.3.3. Determining Damage concentration in hBN for optimum fluence.

When the mean number of vacancies/ion/Å for damage distribution is multiplied by the fluence over the entire region, it gives the damage density/vacancy concentration *C(x)* in the material.

$$C(x) = C_p \times D \tag{5.1}$$

The damage density concentration was determined for our selected ions from the SRIM calculation in figure 5.1.

Table 5.2: Calculated damage density concentration in the material.

Ions	**Optimum fluence (10^{15}ions/cm^2)**	**C_p(vacancies/10^{-8}cm-ion)**	**R_p(Å)**	**C(x)(10^{21} vac/cm^3)**
Helium	6	$1.06\text{x}10^{-2}$	$7.1\text{x}10^{3}$	3.2
Lithium	1	$1.4\text{x}10^{-2}$	$7.5\text{x}10^{3}$	1.4
Boron	0.5	$2.75\text{x}10^{-2}$	$3.7\text{x}10^{3}$	1.4
Neon	4	$4.39\text{x}10^{-2}$	$2.4\text{x}10^{3}$	17

5.4. Ion implantation: varying temperature and ion fluence at 150 keV

Figure 5.12 below shows the graph of temperature as a function of logarithmic fluence. The implantations where done by varying temperature and ion fluence.

It is important to take account of the heating effect of the ion beam as a function of fluence. Energy is delivered as volts x amps (or kV x mA) by the accelerator, and lost from the target mainly by radiation in vacuum, according to the fourth power of its Kelvin temperature, leading eventually to an equilibrium temperature. Some measurements were carried out and are plotted logarithmically in Figure 5.12. Fortunately, most of the fluences of interest here are low, ~10^{15} cm^{-2}, but for greater than 10^{16} cm^{-2} the slightly different realm of Figures 5.10 and 5.11 is being entered. Better target temperature control, or at least measurement, is required; but it is difficult to do this for the very surface.

Although, this was not relevant for this work, it is important to take into account the temperature changes while doing implantations. Table 5.3 shows the fluence and implant temperatures and the temperature difference. Implant temperature T_1 is the temperature set to do implantations and T_2 is the increase in temperature while implantations are done.

Table 5.3: The temperature difference obtained from implantation.

	Helium			**Lithium**		
Fluence (ions/cm^2)	T_1(℃)	T_2(℃)	ΔT(℃)	T_1(℃)	T_2(℃)	ΔT(℃)
1x10^{14}	25	50	25	25	66	41
5x10^{14}	100	114	14	100	133	33
1x10^{15}	150	155	5	150	160	10
5x10^{15}	200	241	41	200	208	8
1x10^{16}	250	276	26	250	286	36
5x10^{16}	300	300	0	300	300	0
	Boron			**Neon**		
Fluence	T_1(℃)	T_2(℃)	ΔT(℃)	T_1(℃)	T_2(℃)	ΔT(℃)
1x10^{14}	25	51	26	25	44	19
5x10^{14}	100	110	10	100	109	9
1x10^{15}	150	160	10	150	162	12
5x10^{15}	200	231	31	200	241	41
1x10^{16}	250	291	41	250	309	59
5x10^{16}	300	305	5	300	390	90

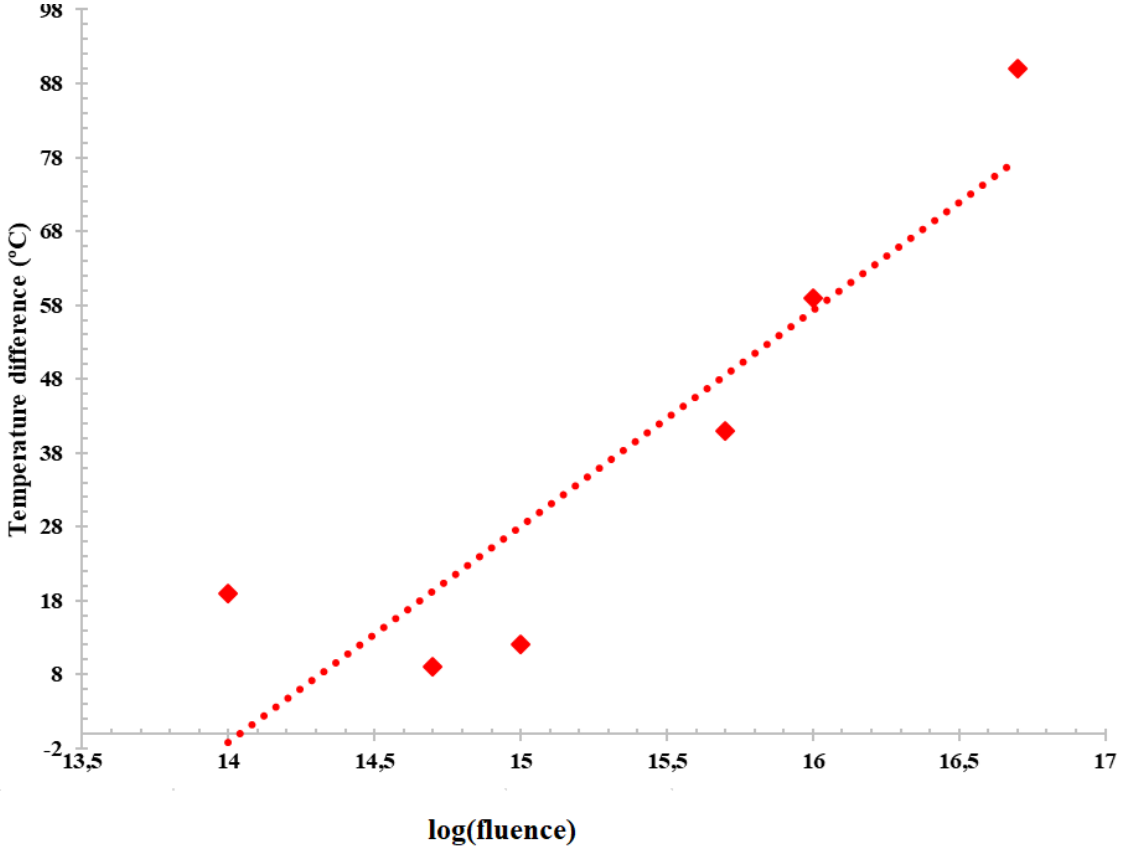

Figure 5.12: Temperature as a function of logarithmic fluence for Ne^{+}.

5.5. Stress, Strain and Young's Modulus

After doing hardness measurements using Vickers micro-indentation, it was important to determine other properties like stress, strain and Young's modulus. The stress calculation was determined from the measured hardness values, and the strain calculations were determined from the measured diagonal distances.

Table 5.4 lists the measured hardness values (HV) for room temperature implants

Table 5.4: The measured hardness values for h-BN samples implanted at room temperature.

Fluence (ions/cm^2)	Log (Fluence)	Helium HV (kg/mm^2)	Lithium HV (kg/mm^2)	Boron HV (kg/mm^2)	Neon HV (kg/mm^2)
0	-	13.4	13.4	13.4	13.4
1x10^{14}	14.0	14.3	13.7	14.7	15.8
5x10^{14}	14.7	15.4	16.1	15.9	17.5
1x10^{15}	15.0	17.2	16.6	18.0	18.7
5x10^{15}	15.7	17.2	15.4	17.7	17.9
1x10^{16}	16.0	14.2	14.0	15.5	16.3
5x10^{16}	16.7	15.7	14.1	14.9	15.8

From Table 5.4, the hardness value has units kg/mm^2 given by equation 4.2. Therefore, the stress is given by the following equation:

$$\sigma = \frac{F}{A}, \tag{5.2}$$

where σ(Pa) is the stress, F(N) is the force applied by a specific load (in this case 100g) and A(m^2) the area caused by the Vickers's indent. For example, the un-implanted sample has zero fluence (ions/cm^2) and has a hardness value of $13.4 \pm 2\ \mathrm{kg/mm^2}$ which can be used to determine the stress in the following way:

$F = mg$ ($\mathrm{kg.\,ms^{-2}}$) , therefore, $13.4 \pm 2\ \mathrm{kg/mm^2}$ can be multiplied by the gravitational constant 9.8 m/s^2 and divided by 1.8544, the constant from equation 4.2.

Thus:

$$\sigma = \frac{9.8m.s^{-2} \times 13.4}{1.8544\ (10^{-6})m^2} \approx 71\ \text{MPa}$$

Figure 4.13 (b) shows the diagonal distances measured by micro-indentation. The strain was determined using the diagonal distances. The average diagonal distance was calculated on an un-implanted region of the sample, d_0, and for implanted regions, d_1 for the first fluence and d_2 for the second one, etc. The strain on the sample was determined by the following equation:

$$\in = \frac{\Delta d}{d_n,} \tag{5.3}$$

where $\in$ is the strain, $\Delta d = d_n - d_0$, n=1, 2, 3...etc. The Young's modulus is determined from the gradient of the stress-strain graph, figure 5.13.

Table 5.5: Determined values of stress, strain and Young's modulus at room temperature from B^+ implantation.

B^+ ions, HV (kg/mm^2)	**σ(MPa)**	**d_n**(mm)	∈	**Y(MPa)**
13.4	71	121	0	-
14.65	77	112,62	0,0692	1117
15.90	84	108,08	0,1067	787
18.00	95	100,80	0,1669	569
17.75	93	102,18	0,1555	603
15.45	81	109,54	0,0947	862
14.90	78	111,58	0,0778	1011

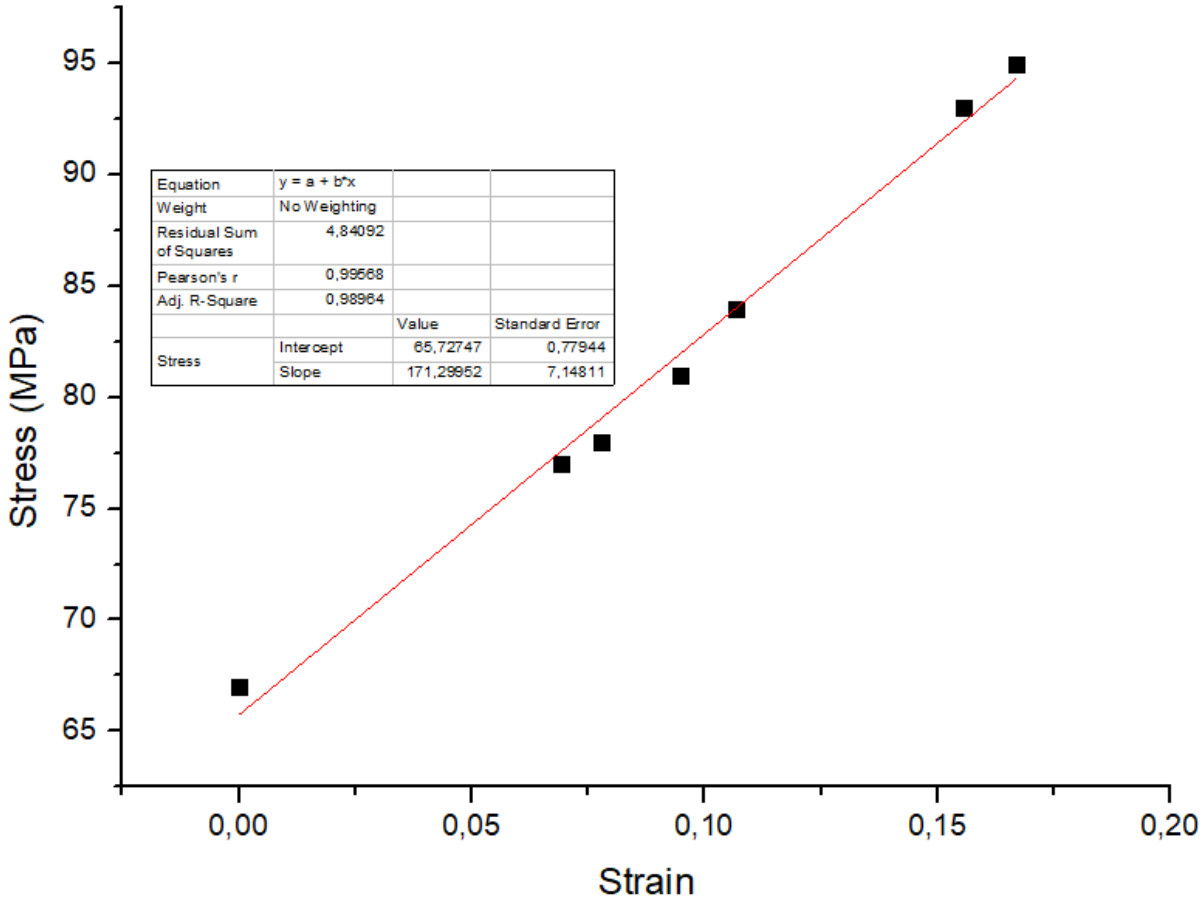

Figure 5.13: The graph of stress as a function of strain (B^+ implantation).

The same method for data analysis was done for all ions (B^+, Li^+, He^+ and Ne^+) at room temperature, 150℃ and 300℃. The tables below contain the summary of the determined Young's moduli and threshold stress (because this is the stress needed to be applied to cause strain on the surface) of the implanted h-BN sample.

Table 5.6: Room Temperature implants.

Ion Beam	Young's Modulus (MPa)	Threshold stress (MPa)
Helium	139±2	74±1
Lithium	156±9	70±0.8
Boron	171±7	65±0.8
Neon	202±3	74±0.3

Table 5.7: 150℃ Temperature implants.

Ion Beam	Young's Modulus (MPa)	Threshold stress (MPa)
Helium	131±2	50±0.9
Lithium	101±2	54±0.7
Boron	137±2	48±0.6
Neon	148±3	46±0.1

Table 5.8: 300℃ Temperature implants.

Ion Beam	Young's Modulus (MPa)	Threshold stress (MPa)
Helium	201±7	39±0.4
Lithium	123±3	51±0.2
Boron	134±2	49±0.8
Neon	129±3	50±0.1

5.6. Glancing Incidence X-ray Diffraction (GIXRD)-Results

The GIXRD spectrum data is in the form of diffraction peak intensity as a function of diffraction angle. If the angle satisfies the Bragg's equation, any material can reflect X-rays at 2θ angle. Diffraction peak patterns are used to identify different planes of a material and they correspond to a certain set of Miller indices which are used to analyze crystal structure properties such as the lattice parameters, thus assisting in the identification of the material.

The analysis was done at a $w_i = 2°$ incident angle and the recording was made from $2\theta = 20°$ to $2\theta = 90°$, in steps of $0.02°$ for a duration of 4 hours. When doing X-ray diffraction, it is important to know the depth of your X-rays into the sample (X-ray depth, X_d). However, when using GIXRD the X-rays are being directed towards the sample in a small angle (GIXRD was used because the implanted layers were very thin around $300 - 600\text{nm}$, see figure 5.1). The X-ray attenuation length (X_L) needed to be calculated (refer to section 5.6.2) in order to be able to determine the X-ray depth. The following equation was then obtained from the geometry of figure 5.14:

$$X_d = X_L \times \tan(w_i) \tag{5.4}$$

$$\therefore X_d = (964\mu m) \times \tan(2°) \sim 34\mu m$$

Because the implanted layer is roughly $\sim 500\text{nm}$, which is the depth we would prefer our X-rays to penetrate, therefore using equation 5.4 we obtain $w_i \sim 0.03°$, this is the angle we would need to obtain great sensitivity from the XRD-spectrum. The X-ray depth, $X_d = 34\mu m$ is 60 times what we want. In this instance, the GIXRD equipment was not able to adjust to $0.03°$ angle, but the $2°$ angle worked because we were able to identify two new peaks on the implanted spectra.

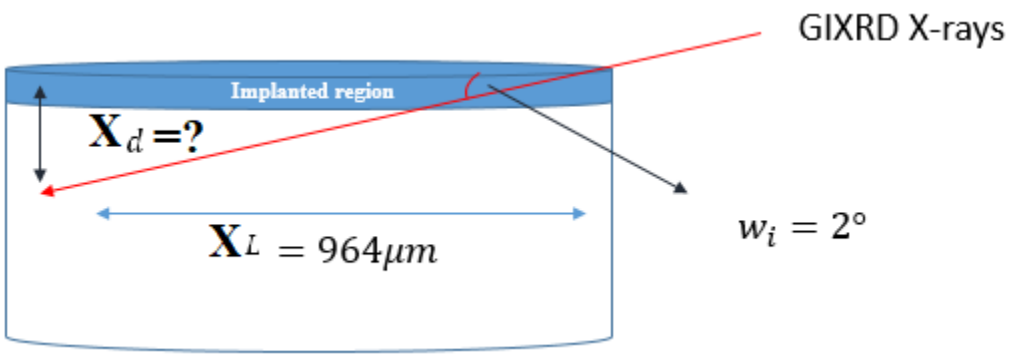

Figure 5.14: A diagram, showing the X-ray attenuation length and X-ray depth for h-BN.

Table 5.9: Experimentally determined X-ray attenuation length and X-ray depth.

	Un-implanted	**Helium**	**Lithium**	**Boron**	**Neon**
Attenuation length (µm)	951	1057	999	995	995
X-ray depth (µm)	33	37	35	35	35

5.6.1. Hexagonal-BN XRD spectra and calculations of lattice parameters before and after implantation.

Figure 5.15 is a GIXRD spectrum of a virgin h-BN sample. The diffraction pattern shows several peaks at Bragg angle values listed in Table 5.10. The peak that has the highest intensity is at 26.72°.

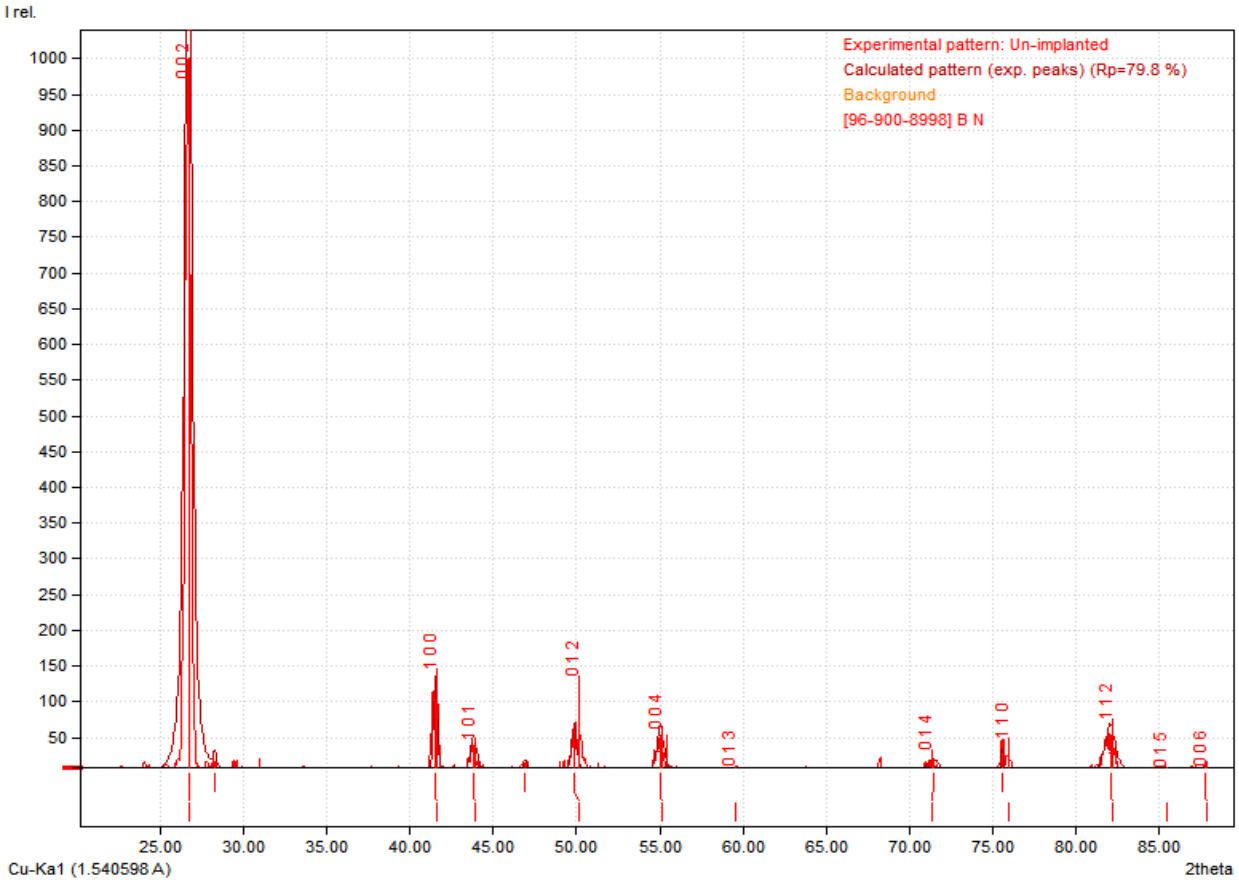

Figure 5.15: The XRD spectrum of un-implanted h-BN.

Figures 5.16 and 5.17 are the h-BN GIXRD spectra of implanted samples. After ion implantation, there are two new un-identified peaks at 28.05° and 46.45° on all implanted samples. The peak at 28.05° is the characteristic silicon (311) diffraction peak which came from the sample holder. The peak at 46.45° is identified as the (111) peak of c-BN from JCPDS database no 35-1365. The plane spacing equation for hexagonal crystal structures is given by the following equation:

$$\frac{1}{d^2} = \frac{4}{3}\left(\frac{h^2+hk+k^2}{a^2}\right) + \frac{l^2}{c^2}, \tag{5.5}$$

Bragg's equation is given by the following expression

$$\lambda = 2d \sin\theta \tag{5.6}$$

Equation 5.6 can be re-written as $\lambda^2 = 4d^2 sin^2\theta$, therefore substituting equation 5.6 into equation 5.5 we obtain the following expression:

$$\sin^2\theta = \left(\frac{\lambda^2}{4a^2}\right)\left[\frac{4}{3}(h^2 + hk + k^2) + \frac{l^2}{(c/a)^2}\right] \tag{5.6}$$

Bragg's law and the plane spacing equation for hexagonal systems give the above expression, where *hkl* are miller indices, *a* and *c* are lattice parameters, λ is the wavelength used for diffraction measurements and θ the diffraction angle.

Match! XRD software [50] was used to plot and index hBN XRD spectra. To determine spectra lattice parameters, first, we need to consider that the lattice parameter *a* and the ratio of the lattice parameters (*c/a*) is constant for a given diffraction pattern, hence the term $\left(\frac{\lambda^2}{4a^2}\right)$ in equation 5.6 is constant. We can thus index by considering $\frac{4}{3}(h^2 + hk + k^2)$ and $\frac{l^2}{(c/a)^2}$. This term $\frac{4}{3}(h^2 + hk + k^2)$ depends only on h and k indices and its value can be determined for different h and k values, meaning *l*=0 (to determine the lattice parameter *a* we only consider indices where *l*=0, i.e. (*hk0*)).

The term $\frac{l^2}{(c/a)^2}$ only depends on *l* indices, meaning (00*l*) and the lattice parameter ratio can be determined. The following Table shows the allowed indices, and the determined lattice parameters for figures 5.15-5.17:

Table 5.10: The determined lattice parameters of h-BN before and after implantation.

Unimplanted sample				Helium implants			Lithium implants			Boron implants			Neon implants		
hkl	2θ	*a*	*c*	2θ	*a*	*c*	2θ	*a*	*c*	2θ	*a*	*c*	2θ	*a*	*c*
100	41.72	2.498		41.36	2.519		41.48	2.512		41.54	2.508		41.54	2.508	
110	76.04	2.501		71.31	2.643		75.56	2.515		75.78	2.508		75.74	2.509	
002	26.72		**6.667**	26.60		**6.697**	26.66		**6.682**	26.66		**6.682**	26.66		**6.682**
004	55.46		**6.611**	49.82		**7.315**	50.00		**7.291**	50.06		**7.282**	50.06		**7.282**
006	88.82		**6.605**	87.68		**6.73**	87.80		**6.665**	87.62		**6.676**	87.80		**6.665**
Average		2.499	**6.628**		2.581	**6.914**		2.514	**6.879**		2.508	**6.880**		2.509	**6.876**
c/a		**2.652**			**2.679**			**2.736**			**2.743**			**2.741**	

Now that we know the lattice parameters and their ratios, we can determine the density of the sample and atomic radius using the following expression

$$\rho = \frac{nA}{V_c N_A}, \tag{5.8}$$

where ρ $\left(\frac{\mathrm{g}}{\mathrm{cm}^3}\right)$ is the density, $A(\mathrm{g.mol}^{-1})$ is the atomic mass, N_A (mol^{-1}) is the Avogadro's constant, $V_c = a^2 c \frac{3\sqrt{3}}{2}$ (cm^3) is the volume and n is the number of atoms in the hexagonal structure. Table 5.11 shows the calculated density and atomic radii of the h-BN sample before and after implantation and where the atomic radius is just half the lattice parameter of h-BN (e.g. $a = 2r$).

Table 5.11: Calculated density and atomic radii of the h-BN sample before and after implantation.

	Un-implanted	**Helium**	**Lithium**	**Boron**	**Neon**
c/a	2,652	2,679	2,736	2,743	2,741
a(Å)	2,499	2,581	2,514	2,508	2,509
Density g/cm^3	**2,30**	**2,07**	**2,19**	**2,20**	**2,20**
atomic radius(Å)	**1,249**	**1,290**	**1,257**	**1,254**	**1,255**

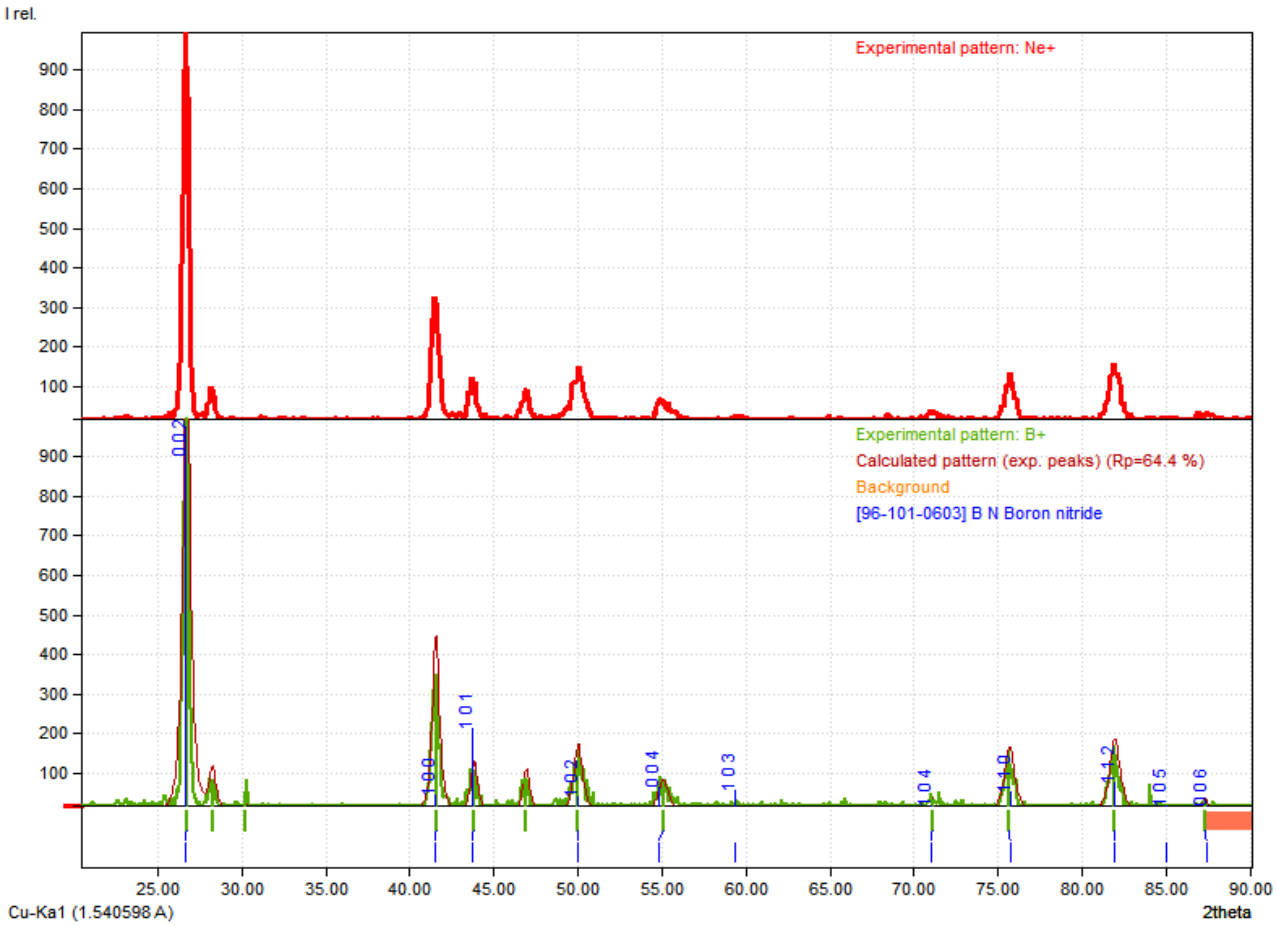

Figure 5.16: XRD Spectra of implanted h-BN samples with B^+ and Ne^+ ions.

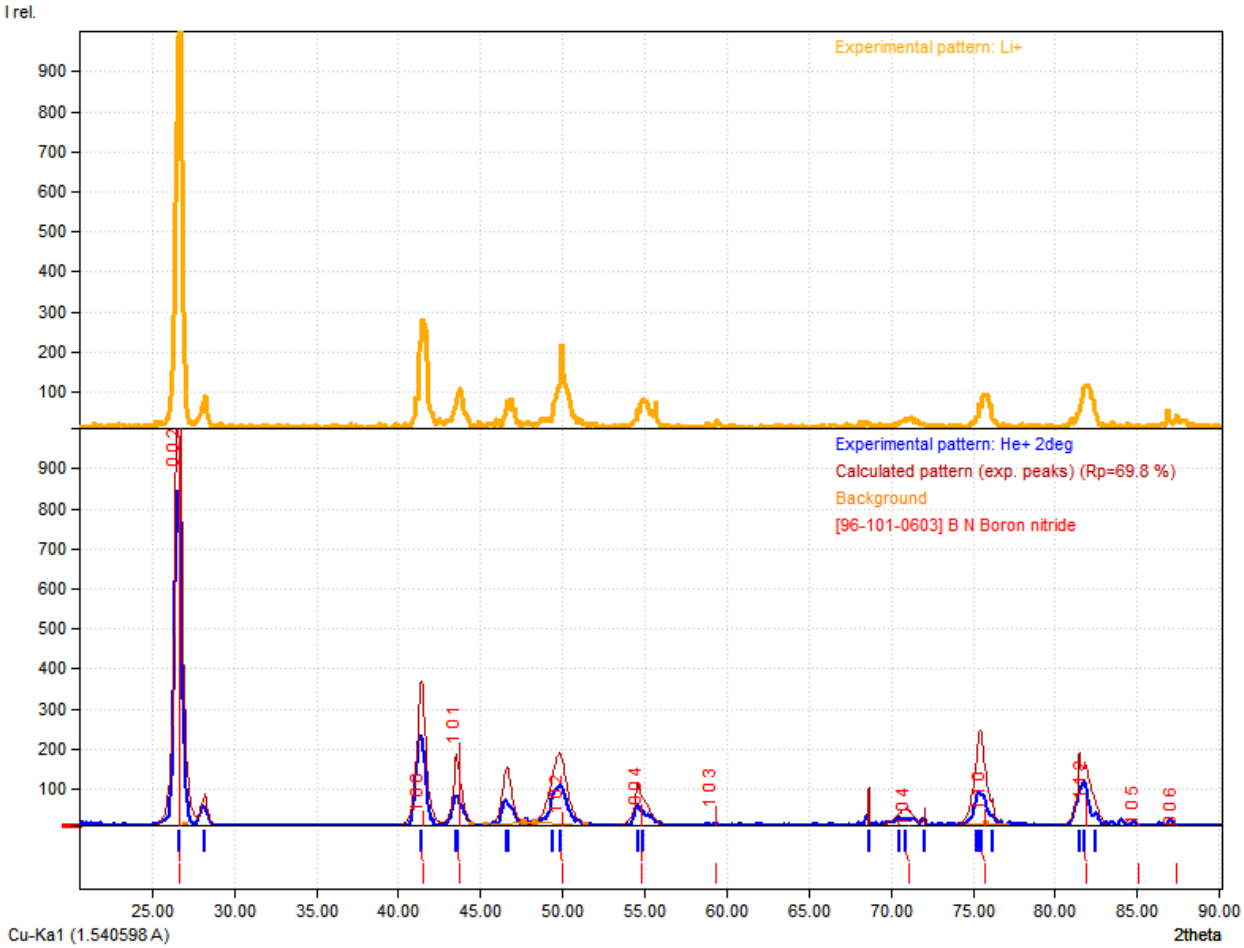

Figure 5.17: XRD Spectra of implanted h-BN samples with Li^+ and He^+ ions.

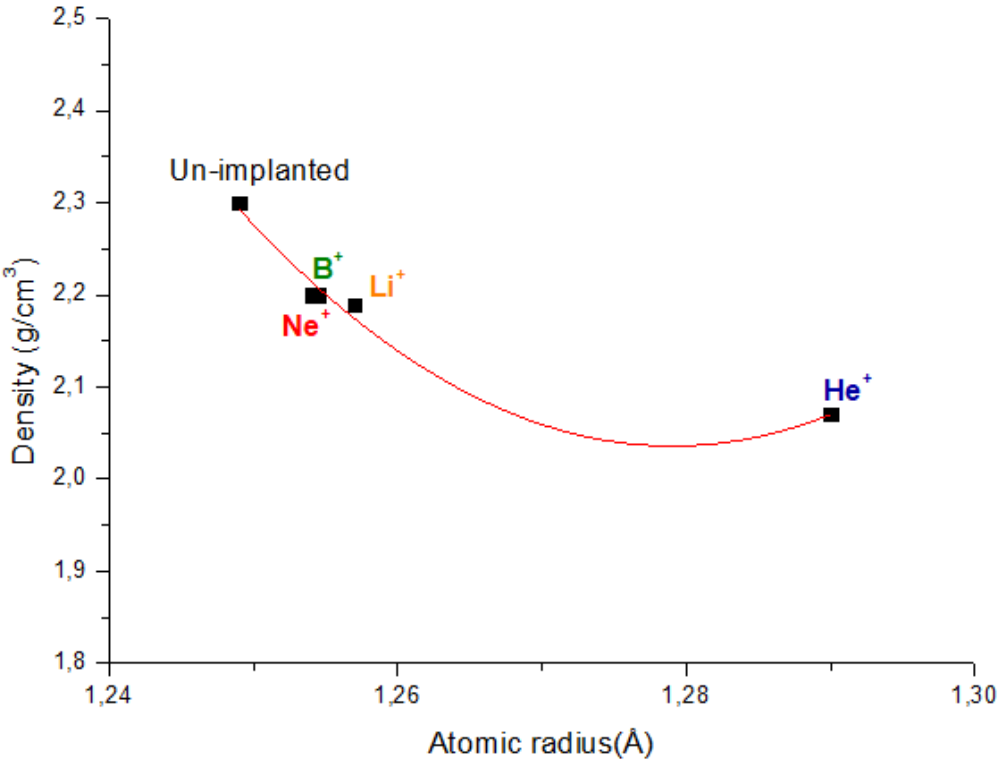

Figure 5.18: Hexagonal BN density as a function of atomic radius before and after implantation.

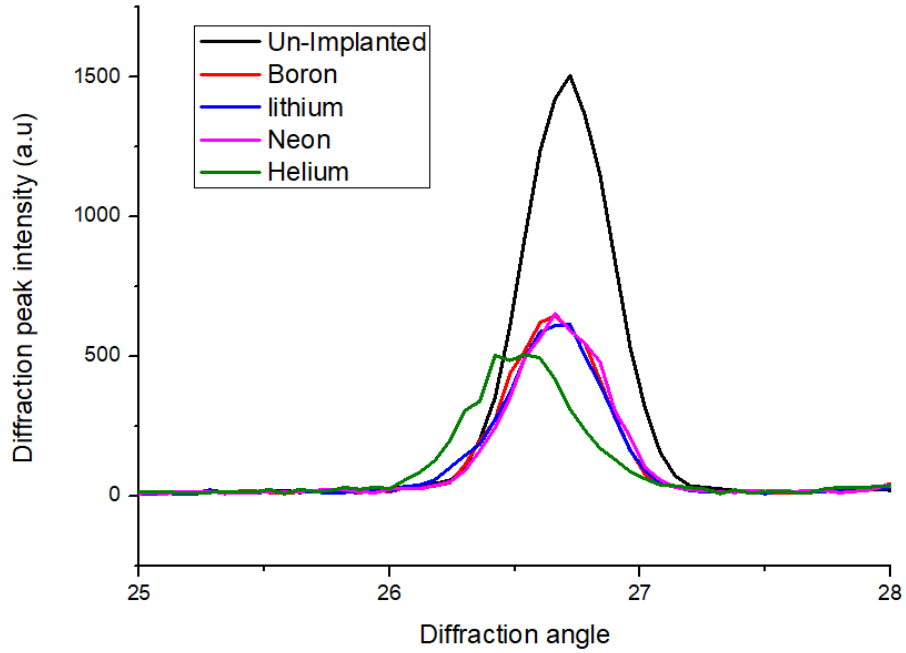

Figure 5.19: XRD spectra showing the peak with the highest intensity at 26.72°.

Figure 5.18 shows density as a function of atomic radius. From the graph it is evident that an increase in atomic radius due to implantation decreases the density of the h-BN sample, and light ions (He^+ and Li^+) have more effect in decreasing the density than heavy ions (B^+ and Ne^+) (see figure 5.2).

Figure 5.19 shows that the intensities of the XRD spectra decrease after ion implantation, and the lighter the ion the lesser the intensity.

There is also a shift in the peak position to lower angles and broadening, this could be the residual stress caused by ion implantation because there is a change in the lattice parameter ratios, i.e. one lattice parameter becomes shorter, the other longer. This could possibly mean a stress-related hexagonal to cubic nanoparticle phase change.

5.6.2. X-Ray Attenuation Length

When a beam of X-rays penetrates through the sample, the intensity of these X-ray photons decreases. The interaction of the photons with the atoms of the sample removes an X-ray from the beam thus causing the intensity to decrease. Attenuation depth is then the depth the X-rays intensity has decreased to 1/e of the value at material surface.

For example, the decrease in intensity depends on the depth of penetration X_d and the materials absorption coefficient (A). The intensity is reduced exponentially, given by the following equation [50]:

$$\frac{\mathrm{I}}{\mathrm{I_0}} = \mathrm{e}^{(-\mathrm{A}X_L)} \tag{5.9}$$

where $\mathrm{I_0}$ is the initial X-ray beam intensity, I the diffracted intensity and X_L the X-Ray attenuation length. The mass absorption coefficient (μ), is related to the absorption coefficient by the density of the material (ρ) as $\mu = \mathrm{A}/\rho$, equation 5.9 can then be written as the Beer–Lambert law:

$$\frac{\mathrm{I}}{\mathrm{I_0}} = \mathrm{e}^{(-\mu\rho X_L)} \tag{5.10}$$

Therefore if $I/I_0 = 1/e$ and substituting this term into equation 5.10, we obtain:

$$X_L = 1/(\mu\rho) \tag{5.11}$$

This is also called the "mean free path" of X-rays.

Polycrystalline hexagonal boron nitride has a density of 2.27g/cm^3 and the Cu$K_{\alpha_1} = 1.540$Å X-ray tube was used. The X-rays photon energy was then 8.051keV. Boron nitride contains 43.56% B and 56.44% N atoms. Therefore, the mass absorption values for the X-ray photon energy of 8.051keV:

$\mu(8.051\text{keV}) = 1.85\text{cm}^2/\text{g}$ for boron and $\mu(8.051\text{keV}) = 6.71\text{cm}^2/\text{g}$ for nitrogen [51] . The total mass coefficient of BN is then the sum of the individual coefficients, each multiplied by the weight fraction present.

$$\mu_s = \sum C_i \mu_i \tag{5.12}$$

Therefore,$\mu_s = C_B\mu_B + C_N\mu_N = (0.44)(1.85\text{cm}^2/\text{g}) + (0.56)(6.71\text{cm}^2/\text{g})$, giving $\mu_s = 4.57\text{cm}^2/\text{g}$ as the absorption mass coefficient for BN.

Substituting μ_s in equation 5.11, we obtain; $X_L = \frac{1}{\mu\rho} = 1/(4.57\text{cm}^2/\text{g})(2.27\text{g/cm3})$. The Attenuation length of X-ray photons is then:

$$\therefore X_L = 964\mu\text{m}$$

Table 5.12 shows the determined X-ray Attenuation Length from the experimentally calculated density values for h-BN using different ions.

Table 5.12: The determined X-ray Attenuation length using the experimentally calculated h-BN density values.

	Un-implanted	**Helium**	**Lithium**	**Boron**	**Neon**
Density (g/cm^3)	2,30	2,07	2,19	2,20	2,20
Attenuation length (μm)	951	1057	999	995	995

Table 5.12, and figure 5.18 below show that when the density of the material is high the X-ray photons penetrate less into the sample.

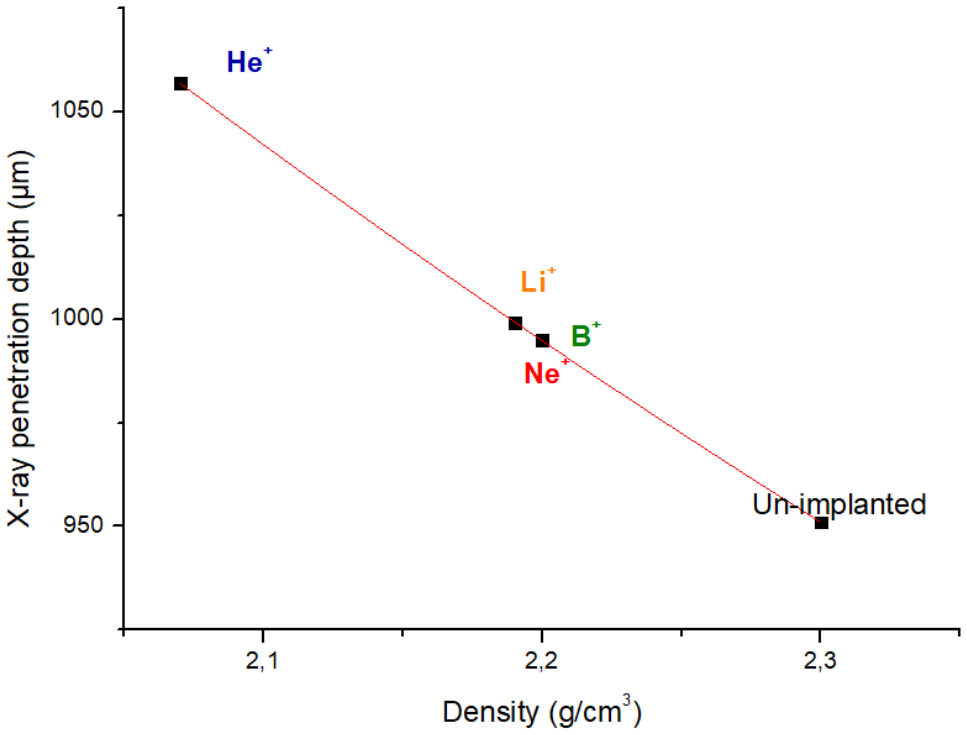

Figure 5.20: The X- Attenuation Length as a function of h-BN density for different implanted ions.

5.6.3. Determining the particle size

The Scherrer equation (5.13) was used to calculate the particle size for the induced c-BN particles. The equation correlates the estimated crystal size ($D_{crystal}$) to the (hkl) plane corresponding to 2θ angle and the linewidth [52].

$$D_{crystal} = \frac{k\lambda}{\beta_{\frac{1}{2}} \cos\theta} \tag{5.13}$$

where λ is the wavelength of the incident X-ray beam, k is the Scherrer′s constant~0.94, $\beta_{\frac{1}{2}}$ the full width at half maximum of the diffraction peak, and θ the Bragg angle for the specific (hkl) plane.

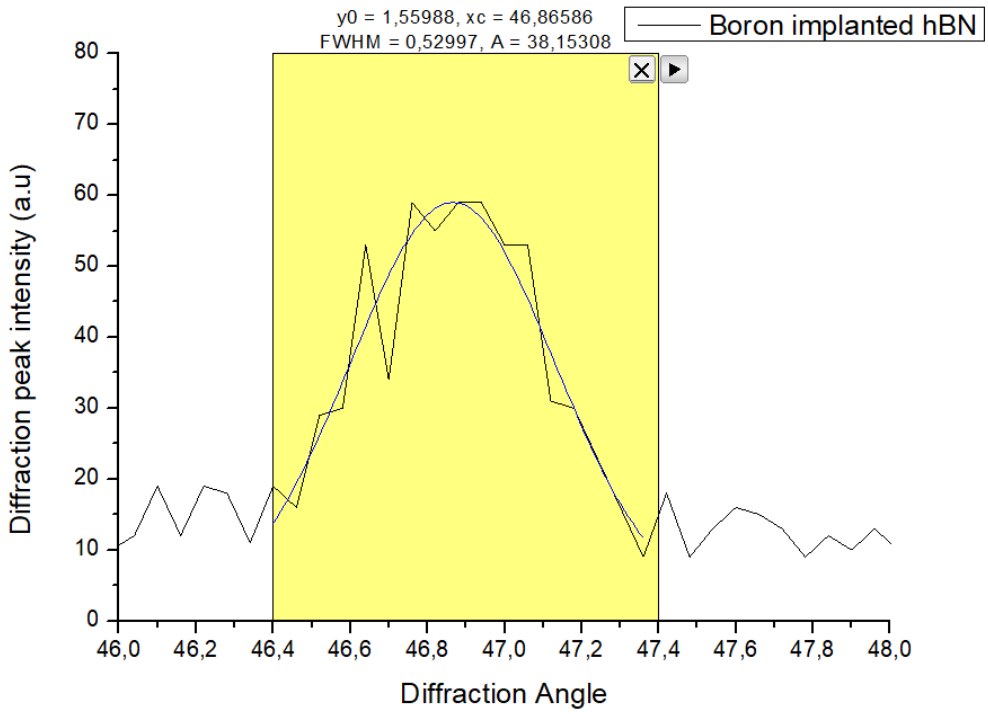

Figure 5.21: The observed X-ray peak at 46.86 º for Boron implanted hBN sample.

The information in figure 5.21 is used to calculate the particle size of the induced c-BN particles on the h-BN sample, $\beta_{\frac{1}{2}} = 0.53$, λ=1.504Å and $\theta = 46.86°$.

$$D_{crystal}(B^{+}) = \frac{0.94 \times 1.504\text{Å}}{0.53 \times \cos(46.86°)} \approx 3.901\text{Å}$$

$$\therefore D_{crystal}(B^{+}) \approx 0.40\text{nm}$$

The determined particle sizes for the rest of the ions are tabulated in Table 5.13.

Table 5.13: The calculated particle size from the XRD-spectra identified peak.

	Helium	**Lithium**	**Boron**	**Neon**
Bragg angle	46.81º	46.60º	46.86º	46.90º
FHWM	0.43	0.62	0.53	0.40
Particle-size (nm)	0.48	0.33	0.40	0.52

CHAPTER 6

6. SUMMARY AND CONCLUSION

This study has investigated changes in hardness on ion beam implanted polycrystalline hexagonal boron nitride (h-BN), using the FM-700 (Vickers) micro-hardness tester. The ion implanted h-BN samples showed a structural phase change from h-BN to c-BN as evidenced from Raman measurements that showed a broad peak around 1300 cm^{-1}. The GIXRD results show that after ion implantation new un-identified peak 46.45° on the XRD spectra of implanted samples. The peak at 46.45° is identified as the (111) peak of c-BN. The lattice parameter of the as-grown h-BN, calculated from the experimental XRD data, was 2.499Å, the parameters of the samples implanted with He^+, Li^+, B^+, and Ne^+ ions were 2.581 Å, 2.514 Å, 2.508 Å and 2.509 Å respectively. The is a shift in the peak position to lower angles and broadening, this is due to the residual stress caused by ion implantation because the is a change of the lattice parameter ratios, i.e. one lattice parameter becomes shorter, the other longer. This could possibly mean is a stress related hexagonal to cubic nanoparticles phase change.The atomic radius of h-BN sample increases due to implantation thus this causes a slight decrease in its density. Light ions (He^+ and Li^+) have more effect in decreasing the density than the heavy ions (B^+ and Ne^+). The measured hardness value of the as-grown h-BN was $13.4 \pm 2\ kg/mm^2$ and the hardness values of the ion beam implanted h-BN varied from $16.03\ kg/mm^2$ to $22.00\ kg/mm^2$. Thus, micro-indentation results confirmed that ion-implantation increases hardness until an optimum hardness is reached then the hardness decreases as the ion fluence increases.

CONFERENCES

- SAIP annual conference June 2017 at Stellenbosch-Poster presentation: Allotrope Conversion and Surface Hardness Increase in Ion Implanted Boron Nitride.

- SAIP annual conference June 2018 at University of the Free State: Properties of boron nitride nano-particles formed by ion implantation.

- International Conference on Ion Beam Modification of Materials (IBMM-2018), San Antonio, Texas, USA, June 24-29, 2018. (Paper accepted but visa refused)

PUBLICATIONS

- Derry, T. E., Lisema, L. I., Magabe, A. T., Aradi, E., Machaka, R., & Madhuku, M. (2018). Allotrope conversion and surface hardness increase in ion implanted boron nitride. *Surface and Coatings Technology* 355 (2018) 61-64.

APPENDIX

Derivation of Vickers hardness number (VHN):

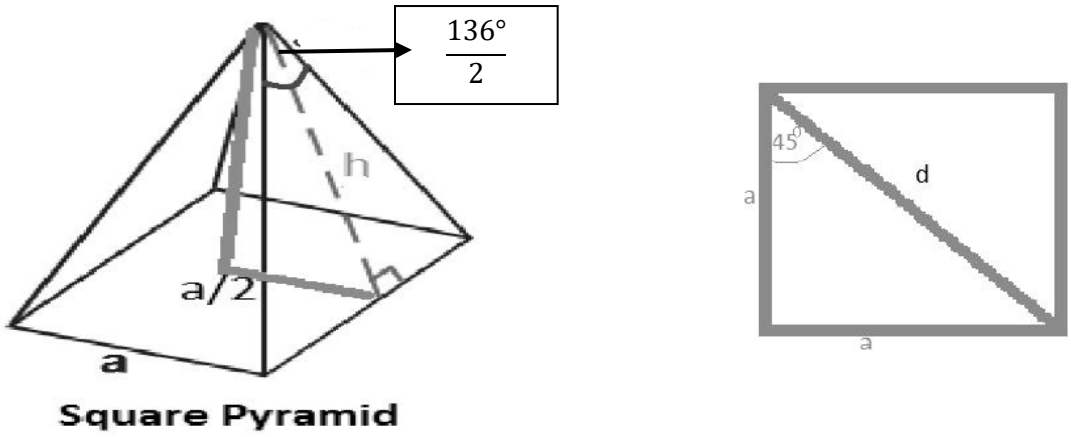

Figure A: square base pyramid shape formed by the indenter.

The indenter forms a square base pyramidal. Therefore, the area (A) is:

$$A = 4(\frac{1}{2}ah) \tag{a}$$

figure A, using trigonometry identities

$$\cos(45°) = \frac{a}{d}$$

$$\therefore a = \frac{d\sqrt{2}}{2} \tag{b}$$

$$h = \frac{a}{2sin(\frac{136°}{2})} \tag{c}$$

Substituting equation (b) and (c) into (a)

$$A = \frac{d^2}{\sin(\frac{136^\circ}{2})} \approx \frac{d^2}{1.8544} \qquad \text{(d)}$$

Therefore, the Vickers hardness number (VHN) is

$$\therefore VHN = \frac{F}{A} \approx \frac{1.8544F}{d^2}$$

BIBLIOGRAPHY

[1] E. Aradi, “Investigations on the characterization of ion implanted hexagonal boron nitride,” University of the Witwatersrand, 2014.

[2] R. Machaka, “Ion Beam Modifications of Boron Nitride by Ion Implantation,” University of the Witwatersrand, 2008.

[3] R. MacHaka, R. M. Erasmus, and T. E. Derry, “Formation of cBN nanocrystals by He+implantation into hBN,” *Diam. Relat. Mater.*, vol. 19, no. 10, pp. 1131–1134, 2010.

[4] E. Aradi, S. R. Naidoo, R. M. Erasmus, B. Julies, and T. E. Derry, “Investigations on the characterization of ion implanted hexagonal boron nitride,” *Nucl. Instruments Methods Phys. Res. Sect. B Beam Interact. with Mater. Atoms*, vol. 307, pp. 214–217, 2013.

[5] E. Aradi, R. M. Erasmus, and T. E. Derry, “Formation of c-BN nanoparticles by helium, lithium and boron ion implantation,” *Nucl. Instruments Methods Phys. Res. Sect. B Beam Interact. with Mater. Atoms*, vol. 272, pp. 57–60, 2012.

[6] J. Griggs, “Diamond no longer nature’s hardest material.” [Online]. Available: www.newscientist.com/article/dn16610-diamond-no-longer-natures-hardest-material. [Accessed: 28-Aug-2018].

[7] B. Andrzej R., “Superhard material comparable in hardness to diamond,” vol. 2495, no. May 1988, pp. 17–20, 2007.

[8] P. B. Mirkarimi, K. F. McCarty, and D. L. Medlin, “Review of advances in cubic boron nitride film synthesis,” *Mater. Sci. Eng. R Reports*, vol. 21, no. 2, pp. 47–100, 1997.

[9] D. J. Kester and R. Messier, “Phase control of cubic boron nitride thin films,” vol. 504, no. June, 1998.

[10] V. Z. Turkevich, “Phase diagrams and synthesis of diamond,” *High Press. Res.*, vol. 22, no. 3–4, pp. 525–529, 2002.

[11] S. K. Klitgaard, “Turbostratic Boron Nitride Coated on High-Surface Area Metal Oxide Templates,” *Eur. J. Inorg. Chem.*, vol. 31, pp. 4873–4876, 2007.

[12] C. Ronning, H. Feldermann, and H. Hofsäss, “Growth, doping and applications of cubic boron nitride thin films,” *Diam. Relat. Mater.*, vol. 9, no. 9–10, pp. 1767–1773, 2000.

[13] G. Lynn Wood, J. F. Janik, M. Z. Visi, D. M. Schubert, and R. T. Paine, “New borate precursors for boron nitride powder synthesis,” *Chem. Mater.*, vol. 17, no. 7, pp. 1855–1859, 2005.

[14] M. Basu, A. K., Joydeb, “Synthesis of Boron nitride,” vol. 831, no. 1937, pp. 1753–1754, 1961.

[15] V. Kreibig, Y. Parpia, K. Binder, L. Kleinman, and M. Bylander, “Siesta-KB projector.pdf,” vol. 48, no. 20, pp. 1425–1428, 1982.

[16] Y. Al-Douri, “Structural phase transition of boron nitride compound,” *Solid State Commun.*, vol. 132, no. 7, pp. 465–470, 2004.

[17] V. L. Solozhenko, “New concept of BN phase diagram: an applied aspect,” *Diam. Relat. Mater.*, vol. 4, no. 1, pp. 1–4, 1994.

[18] V. L. Solozhenko, “Current trends in the phase diagram of boron nitride,” *J. Hard Mater 6*, vol. 1995, pp. 51–65.

[19] N. Ooi, A. Rairkar, L. Lindsley, and J. B. Adams, “Electronic structure and bonding in hexagonal boron nitride,” *J. Phys. Condens. Matter*, vol. 18, no. 1, pp. 97–115, 2006.

[20] I. Bello *et al.*, “Cubic boron nitride films for industrial applications,” *Diam. Relat. Mater.*, vol. 14, no. 11–12, pp. 1784–1790, 2005.

[21] C. Oshima and A. Nagashima, “Ultra-thin epitaxial films of graphite and hexagonal boron nitride on solid surfaces This article has been downloaded from IOPscience . Please scroll down to see the full text article . Ultra-thin epitaxial films of graphite and hexagonal boron nitride on,” *J. Phys. Condens. Matter*, vol. 9, pp. 1–20, 1997.

[22] L. Liu, Y. P. Feng, and Z. X. Shen, “Structural and electronic properties of *h* -BN,” *Phys. Rev. B*, vol. 68, no. 10, p. 104102, 2003.

[23] L. Vel, G. Demazeau, and J. Etourneau, “Cubic boron nitride: synthesis, physicochemical properties and applications,” *Mater. Sci. Eng. B*, vol. 10, no. 2, pp. 149–164, 1991.

[24] J. Lam and J. F. Lutsko, “Reports on Progress in Physics Related content High-pressure phases of group IV and III-V semiconductors High-pressure phases of group IV and III – V,” 2001.

[25] F. P. Bundy and R. H. Wentorf, “Direct Transformation of Hexagonal Boron Nitride to Denser Forms,” vol. 1144, no. 1963, pp. 1–7, 2007.

[26] J. Robertson, “Deposition mechanism of cubic boron nitride,” *Diam. Relat. Mater.*, vol. 5, pp. 519–524, 1996.

[27] A. Twardowska, “Ion beam assisted deposition of Ti – Si – C thin films,” vol. 37, no. 1, pp. 87–90, 2009.

[28] H. Huang, J.Y., Yasuda, H. and Mori, “HRTEM and EELS studies on the amorphization of hexagonal boron nitride induced by ball milling,” *J. Am. Ceram. Soc.*, vol. 83.2, pp. 403–409, 2000.

[29] J. . Huang and Y. . Zhu, “Advances in the synthesis and characterization of boron nitride,” *Defect Diffus. Forum*, vol. 186, 200AD.

[30] H. Hofsäss, H. Feldermann, M. Sebastian, and C. Ronning, “Thresholds for the phase formation of cubic boron nitride thin films,” *Phys. Rev. B - Condens. Matter Mater. Phys.*, vol. 55, no. 19, pp. 13230–13233, 1997.

[31] V. S. Kharlamov, D. V. Kulikov, and Y. V. Trushin, “Computer simulation of transition from h-BN to c-BN during ion beam assisted deposition,” *Vacuum*, vol. 52, no. 4, pp. 407–410, 1999.

[32] Q. Li, S. F. Wong, W. M. Lau, and C. W. Ong, “Study of the surface layer in cBN growth by PVD techniques,” *Diam. Relat. Mater.*, vol. 16, no. 3, pp. 421–424, 2007.

[33] K. Matsumoto, S, Akashi and K. Sugai, “Preparation of BN films by rf thermal plasma chemical vapour deposition.,” *J. Mater. Sci.*, vol. 31, pp. 713–720, 1996.

[34] J. Yu, Z. Zheng, H. C. Ong, K. Y. Wong, S. Matsumoto, and W. M. Lau, "Thermal stability of cubic boron nitride films deposited by chemical vapor deposition.," *J. Phys. Chem. B*, vol. 110, no. 42, pp. 21073–21076, 2006.

[35] Y. N. Osetsky, D. J. Bacon, B. N. Singh, and B. Wirth, "Atomistic study of the generation, interaction, accumulation and annihilation of cascade-induced defect clusters," *J. Nucl. Mater.*, vol. 307–311, no. 2 SUPPL., pp. 852–861, 2002.

[36] R. A. Spits, T. E. Derry, J. F. Prins, and J. P. F. Sellschop, "Depth profiling of implanted 13C in diamond as a function of implantation temperature," *Nucl. Inst. Methods Phys. Res. B*, vol. 51, no. 3, pp. 247–252, 1990.

[37] J. F. Ziegler, *Ion Implantation Science and Technology*, Second Edi. 1988.

[38] P. Sigmund, "Theory of sputtering. I. Sputtering yield of amorphous and polycrystalline targets," *Phys. Rev.*, vol. 42, no. 3, pp. 494–511, 1969.

[39] G. Spitzlsperger, "Very brief Introduction to Ion Implantation for Semiconductor Manufacturing," 2003.

[40] M. Backman, *Effect of Nuclear and Electronic Stopping Power on Ion Irradiation of Silicon-based Compounds*. 2012.

[41] "Ion implantation." [Online]. Available: www.slideshare.net/bhargavveepuri/81-microtech-ion-implant12. [Accessed: 27-Aug-2018].

[42] T. Hlatshwayo, "Diffusion of silver in 6H-SiC," University of Pretoria, 2010.

[43] P. W. Roos, "Ion sputtering in surface analysis," 2013.

[44] M. . Nastasi and J. . Mayer, *Ion implantation and synthesis of materials*. 2006.

[45] G. K. Hirvonen, J.K., Carosella, C.A. and Hubler, "Production of high-current metal ion beams," vol. 189, pp. 103–106, 1981.

[46] J. . Plummer, M. . Deal, and P. . Griffin, "Silicon VLSI technology," 2000.

[47] J. A. Adibi, B., England, J. G., Moffatt, S., & Marin, "United States Patent (19)," *U.S. Pat. No. 5,883,391. Washington, DC U.S. Pat. Trademark Off.*, no. 19, 1999.

[48] “Hardness Testin.” [Online]. Available: http://web.itu.edu.tr/~arana/hardness.pdf. [Accessed: 14-Nov-2018].

[49] B. E. Warren, “X-ray diffraction,” 1990.

[50] Y. K. Liu, Jodi, Robert E. Saw, “Calculation of effective penetration depth in X-ray diffraction for pharmaceutical solids,” *J. Pharm. Sci.*, vol. 99.9, pp. 3807–3814, 2010.

[51] Spectroscopy Editors, “Attenuation of X-Rays By Matter,” *Spectroscopy*, vol. 20, no. 9, 2005.

[52] A. Taylor, *X-ray metallography*. New York: Wiley, 1961. - 993 p.